The effect of interstitial pressure on tumor growth: coupling with the blood and lymphatic vascular systems

Min Wu[a], **Hermann B. Frieboes**[b], **Steven R. McDougall**[c], **Mark A.J. Chaplain**[d], **Vittorio Cristini**[e], and **John Lowengrub**[a,f,*]

[a]Department of Mathematics, University of California, Irvine

[b]Department of Bioengineering and James Graham Brown Cancer Center, University of Louisville

[c]Institute of Petroleum Engineering, Heriot-Watt University, Edinburgh, Scotland, UK

[d]Division of Mathematics, University of Dundee, Dundee, Scotland, UK

[e]Departments of Pathology and Chemical Engineering, University of New Mexico, Albuquerque

[f]Biomedical Engineering Department, University of California, Irvine

Abstract

The flow of interstitial fluid and the associated interstitial fluid pressure (IFP) in solid tumors and surrounding host tissues have been identified as critical elements in cancer growth and vascularization. Both experimental and theoretical studies have shown that tumors may present elevated IFP, which can be a formidable physical barrier for delivery of cell nutrients and small molecules into the tumor. Elevated IFP may also exacerbate gradients of biochemical signals such as angiogenic factors released by tumors into the surrounding tissues. These studies have helped to understand both biochemical signaling and treatment prognosis. Building upon previous work, here we develop a vascular tumor growth model by coupling a continuous growth model with a discrete angiogenesis model. We include fluid/oxygen extravasation as well as a continuous lymphatic field, and study the micro-environmental fluid dynamics and their effect on tumor growth by accounting for blood flow, transcapillary fluid flux, interstitial fluid flow, and lymphatic drainage. We thus elucidate further the non-trivial relationship between the key elements contributing to the effects of interstitial pressure in solid tumors. In particular, we study the effect of IFP on oxygen extravasation and show that small blood/lymphatic vessel resistance and collapse may contribute to lower transcapillary fluid/oxygen flux, thus decreasing the rate of tumor growth. We also investigate the effect of tumor vascular pathologies, including elevated vascular and interstitial hydraulic conductivities inside the tumor as well as diminished osmotic pressure differences, on the fluid flow across the tumor capillary bed, the lymphatic drainage, and the IFP. Our results reveal that elevated interstitial hydraulic conductivity together with poor lymphatic function is the root cause of the development of plateau profiles of the IFP in the tumor, which have been observed in experiments, and contributes to a more uniform distribution of oxygen, solid tumor pressure and a broad-based collapse of the tumor lymphatics. We also find that the rate that IFF is fluxed into the lymphatics and host tissue is largely controlled by an elevated vascular hydraulic conductivity in the tumor. We discuss the implications of these results on microenvironmental transport barriers, and the tumor invasive and metastatic potential. Our

results suggest the possibility of developing strategies of targeting tumor cells based on the cues in the interstitial fluid.

1 Introduction

Vascularized tumor growth is a complex process spanning a wide range of spatial and temporal scales, and involves inter-related biophysical, chemical and hemodynamic factors in the interplay between tumor formation, vascular remodeling, and angiogenesis. In the early stages of carcinogenesis, tumor cells are believed to be supported by the pre-existing vasculature sustaining the normal tissue. red These factors remodel the surrounding pre-existing vessel network without necessarily generating new vessels (e.g., by cooption and circumferential growth (Holash *et al.*, 1999*a*; Holash *et al.*, 1999*b*)). The secretion of TAF also leads to tumor-induced angiogenesis as the vasculature becomes unable to support the increasing number of tumor cells, causing new blood vessels to form from the pre-existing vascular network (Raza *et al.*, 2010; Folkman, 1971) through endothelial cell sprouting, proliferation, anastomosis, and remodeling. These processes enable oxygen and cell nutrients circulating in the vasculature to be transported and released closer to the hypoxic tumor cells. However, the interaction between tumor cells and the surrounding vasculature is abnormal due to inadequate signaling from the tumor cells, leading to the creation of new vessels that are inefficient, tortuous and leaky (De Bock *et al.*, 2011; Greene & Cheresh, 2009; Hashizume *et al.*, 2000; Jain, 2001). In order to elucidate these complex processes from a biophysical perspective, modeling of vascularized tumor growth has been an important focus in mathematical oncology, red e.g., see the recent reviews (Byrne, 2010; Lowengrub *et al.*, 2010; Frieboes *et al.*, 2011; Roose *et al.*, 2007; Astanin & Preziosi, 2007; Harpold *et al.*, 2007; Anderson & Quaranta, 2008; Deisboeck & Couzin, 2009; Ventura & Jacks, 2009).

Two critical components in tumor growth and vascularization are the interstitial fluid pressure (IFP) and the interstitial fluid flow (IFF) in the tumor and surrounding tissues. Mathematical models of IFP and macromolecule transport were pioneered in (Baxter & Jain, 1989) under several simplifying assumptions including radial symmetry and spatially uniform blood vessel distributions and intravascular pressures. The models demonstrated that in steady-state, the IFP attains a plateau profile in which the IFP is high and nearly constant in the tumor interior and drops to a lower value near the tumor boundaries and surrounding host tissues. Accordingly, there is little IFF in the tumor interior whereas near the tumor boundary, the IFF is mainly directed outward towards the surrounding tissue. Experimentally, such plateaus of IFP have been observed in tumor samples (Lunt *et al.*, 2008; Milosevic *et al.*, 2008; Boucher *et al.*, 1990). An increase in IFP has been implicated in the development of barriers to the transport of drugs and macromolecules in the tumor microenvironment (Ferretti *et al.*, 2009; Jain, 1987*a*; Jain, 1987*b*). This has led to the concept of vascular normalization to reduce IFP and to decrease transport barriers to improve drug penetration into tumors (Jain, 2001; Jain, 2005*b*; Tong *et al.*, 2004; Jain *et al.*, 2007). Further, other biological factors in the tumor microenvironment, such as TAFs (Phipps & Kohandel, 2011) and *CCR*7 ligands (Shields *et al.*, 2007), can be convected by the interstitial fluid flow similar to drug molecules, which indicates that IFP and IFF may also play an important role in biochemical signaling (Shieh & Swartz, 2011). IFF may also promote tumor invasion via autologous chemotaxis up gradients of *CCR*7 ligands (Shields *et al.*, 2007). In order to predict tumor progression and response to therapy, it is therefore necessary to model and simulate both IFP and IFF.

Recently, mathematical models have been developed to investigate the role of IFP and IFF on the transport of TAFs and tumor-induced angiogenesis and on the chemotaxis of tumor cells in response to gradients of various ligands. For example, (Phipps & Kohandel, 2011)

assumed that TAFs were convected with the IFF using Darcy's law as the constitutive assumption relating IFP with IFF, and a simplified measure of angiogenic activity (Stoll *et al.*, 2003) was used. It was found that under the conditions of spherical symmetry and a fixed tumor radius, the highest TAF concentrations were located in the tumor interior, angiogenesis was suppressed in the tumor core, and angiogenic activity was greatest near the tumor boundary, consistent with experimental observations (Endrich *et al.*, 1979; Fukumura *et al.*, 2001). In (Shields *et al.*, 2007), a Darcy-Stokes (Brinkman) model was used to simulate the velocity field around a single cell to investigate the effect of IFF on gradients of *CCR*7. It was found that IFF could increase the gradient by approximately a factor of three compared to pure diffusive transport. red Recently, IFP, IFF and vascularized tumor growth were coupled dynamically in a model developed by (Cai *et al.*, 2011). Here, we extend this line of research by incorporating a lymphatic system and a pre-existing vasculature.

In recent work (Macklin *et al.*, 2009), we developed a model of vascularized tumor growth following a strategy pioneered by (Zheng *et al.*, 2005) and further developed by red (Bartha & Rieger, 2006; Lee *et al.*, 2006*a*; Welter *et al.*, 2008; Welter *et al.*, 2009; Welter *et al.*, 2010; Frieboes *et al.*, 2010). In particular, we coupled a continuum model of solid tumor progression (Cristini *et al.*, 2003; Zheng *et al.*, 2005; Macklin & Lowengrub, 2008), which accounts for cell-cell, cell-ECM adhesion, ECM degradation, tumor cell migration, proliferation, and necrosis, together with an angiogenesis model (Anderson & Chaplain, 1998; Pries *et al.*, 1998; Pries *et al.*, 1992; McDougall *et al.*, 2002; Stephanou *et al.*, 2005; McDougall *et al.*, 2006; Pries *et al.*, 2009), which incorporates sprouting, branching and anastomosis, endothelial cell (EC) proliferation and migration, blood flow and vascular network remodeling. red The tumor and angiogenesis models were coupled via oxygen extravasated from vessels and TAFs secreted by tumor cells. Oxygen, which represented the total effects of growth-promoting factors, was assumed to affect the phenotype of tumor cells and secretion of TAFs. In particular, hypoxic tumor cells were assumed to secrete TAFs, which initiated sprouting and branching in the vasculature. Once newly formed vessels anastomosed (looped), blood was able to flow through the neo-vascular network, which was modeled using a non-Newtonian Poiseuille law. Stresses induced by the growing tumor and blood flow, were assumed to induce remodeling of the vascular network.

In this paper, we extend this previous model to account for (i) IFP and IFF; (ii) lymphatic vessels and drainage; and (iii) transcapillary interstitial fluid flow (e.g., vessel leakage). We model the lymphatic vessels using a continuum approach. We do not model the process of lymphangiogenesis – see (Friedman & Lolas, 2005; Pepper & Lolas, 2008) for such models – but instead we model the lymphatic drainage capacity, which is affected by the hydrostatic tumor pressure and the degradation of ECM by matrix degrading enzymes (MDE). We investigate how nonlinear interactions among the vascular and lymphatic networks and proliferating tumor cells influence IFP, IFF, transport of oxygen, and tumor progression. We also investigate the consequences of tumor-associated pathologies such as elevated vascular hydraulic conductivities and decreased osmotic pressure differences.

The outline of the paper is as follows. In Sec. 2 we present the mathematical models, and describe the numerical algorithm and parameter choices in Sec. 3. Then we present the results in Sec. 4 and discuss them in Sec. 5. In the appendices, we present modeling details regarding microenvironmental interactions (Appendix A) and TAFs (Appendix B).

2 The Mathematical Model

In this section, we present the coupled systems of equations for tumor growth, IFF and IFP, lymphatic vessels and drainage, and angiogenesis and intravascular flow. We describe each system and the coupling between them.

2.1 The Tumor Progession Model

Following (Macklin *et al.*, 2009), we divide the tumor Ω into three regions: the proliferating region Ω_P where the tumor cells have sufficient oxygen levels for proliferation; a hypoxic region Ω_H where the oxygen levels are sufficient for the cells to survive (above the threshold σ_N) but not enough to sustain normal metabolic activity (below the threshold σ_H); and a necrotic region Ω_N where the oxygen level is so low (below the threshold σ_N) that the tumor cells die and are degraded. We also track the necrotic core and its interface Σ_N. See Fig. 1.

2.1.1 Oxygen Transport—The transport of oxygen, nutrients and growth factors (here generically referred to as "oxygen") is modeled by a quasi-steady reaction-diffusion equation (for the oxygen concentration σ), since oxygen is transported much faster than the characteristic time for cell proliferation. We assume that oxygen is supplied by the pre-existing vasculature and the neo-vasculature at the rate λ_{vasc}^{σ}, diffuses into the host and cancerous tissues with diffusivity coefficient D_σ, is uptaken by normal cells with rate λ_{host} and proliferating and hypoxic tumor cells with rates λ_σ and λ_{hyp}, and degrades with rate λ_{nec} in the necrotic core. Accordingly, the equations are given by (Macklin *et al.*, 2009):

$$0 = \nabla \cdot (D_\sigma \nabla \sigma) - \lambda^\sigma(\sigma)\sigma + \lambda_{vasc}^\sigma(\mathbf{x}, t, 1_{vessel}, P_f, \sigma, h) \quad (1)$$

$$\lambda^\sigma = \begin{cases} \lambda_{host}^\sigma & \text{outside } \Omega \\ \lambda_{prolif}^\sigma & \text{in } \Omega_P \\ \lambda_{hyp}^\sigma & \text{in } \Omega_H \\ \lambda_{nec}^\sigma & \text{in } \Omega_N \end{cases} \quad (2)$$

The oxygen supplied by the vascular network is modeled as:

$$\lambda_{vasc}^\sigma = \overline{\lambda}_{vasc}^\sigma \mathbf{1}_{vessel}(\mathbf{x}, t) \left(\frac{h}{\overline{H}_D} - \overline{h}_{min} \right)^+ (1 - k_{P_f} \frac{P_f}{P_e})(1 - \sigma), \quad (3)$$

where $\overline{\lambda}_{vasc}^\sigma$ is an overall transfer rate, $\mathbf{1}_{vessel}$ denotes the characteristic function of the vascular network (e.g., equals 1 at the locations of the vessels and otherwise equals 0), h is the hematocrit in the blood, $\overline{H}_D$ and $\overline{h}_{min}$ are the normal value of hematocrit in the blood and the minimum hematocrit needed to extravasate oxygen, respectively. The positive part is denoted by +. In addition, P_f is the IFP, P_e is an effective pressure (see below in Sec. 2.1.3), and k_{P_f} measures the sensitivity of the vessels to IFP. Eq. (3) is very similar to that used previously in (Macklin *et al.*, 2009) with the exception that the IFP regulates oxygen extravasation instead of the hydrostatic tumor pressure which was used in (Macklin *et al.*, 2009). red Here, the hydrostatic tumor pressure affects oxygen extravasation indirectly through collapse of blood vessels and the resultant change in blood flow. On the other hand, IFP may affect oxygen extravasation by impeding the transcapillary fluid flux that carries oxygen. Note that oxygen may also be delivered via transcapillary diffusion. In Eq. (3), these effects are combined, and we characterize the strength of feedback from the IFP on oxygen extravasation with the parameter k_{P_f} We discuss the effect of IFP on oxygen extravasation further in Sec. 5. Finally, no-flux boundary conditions $\frac{\partial \sigma}{\partial n} = 0$ are used in the far-field.

2.1.2 Tumor Mechanics and the Cell Velocity—The interaction between the tumor cells, the ECM and host cells is influenced by a combination of forces which contribute to the cell velocity field. The proliferating tumor cells generate hydrostatic stress that also

exerts a force on the ECM and host cells. The cells respond to pressure variations by overcoming cell-cell and cell-ECM adhesion and may move passively (pushed by proliferating cells), and actively (via chemotaxis and haptotaxis) through the interstitial space. The ECM may also deform, degrade and remodel in response to pressure and to enzymes released by the cells. Following previous work (Macklin & Lowengrub, 2005; Macklin & Lowengrub, 2006; Macklin & Lowengrub, 2007; Macklin & Lowengrub, 2008; Macklin *et al.*, 2009), we assume that cellular motion within the ECM can be described as an incompressible fluid in a porous medium. Thus, the cell velocity may be modeled as being proportional to all forces following Darcy's law. We also model all the solid phases (including ECM) as moving with a single cellular velocity field. Accordingly, the velocity is given by:

$$\mathbf{v}_c = -\mu \nabla P_c + \chi_E \nabla E \quad (4)$$

where P_c is the hydrostatic tumor pressure, μ is the cell-mobility, which models the net effects of cell-cell and cell-matrix adhesion, E is the ECM density (e.g. non-diffusible matrix macromolecules such as fibronection, collagen or laminin) and χ_E is the haptotaxis coefficient. In Eq. (4), the first term models the passive, hydrostatic pressure-induced motion while the second models active, haptotaxis movement. We do not consider chemotaxis here. Assuming that the density of cells is constant in the proliferating region of the tumor, we may associate the growth of the tumor with the rate of volume change:

$$\nabla \cdot \mathbf{v}_c = \lambda_p, \quad (5)$$

where λ_p is the net proliferation rate. Together with Eq. (4), the hydrostatic pressure satisfies:

$$-\nabla \cdot (\mu \nabla P_c) = \lambda_p - \nabla \cdot (\chi_E \nabla E). \quad (6)$$

We assume that the rate of cell mitosis in the proliferating region is proportional to the amount of oxygen present and that apoptosis may occur. We also assume volume loss may occur in the necrotic region and that there is neither proliferation nor apoptosis in the host tissue and hypoxic regions:

$$\lambda_p = \begin{cases} 0 & \text{outside } \Omega \\ \sigma - A & \text{in } \Omega_P \\ 0 & \text{in } \Omega_H \\ -G_N & \text{in } \Omega_N \end{cases}, \quad (7)$$

where A is the apoptosis rate and G_N is the rate of volume loss in the necrotic core, assuming water is removed and cellular debris is degraded constantly. Cell-cell adhesion can be modeled as a surface tension-like jump boundary condition at the interface Σ between the host and tumor regions, assuming a uniform cell–cell adhesion throughout the tumor:

$$[P_c] = (P_{c,inner} - P_{c,outer}) = \frac{1}{G}\kappa, \quad (8)$$

where G is a parameter that represents the strength of cell-cell adhesion of the tumor and κ is the mean curvature of the interface. At the necrotic boundary Σ_N, we assume P_c and $\mathbf{v}_c$ are continuous :

$$[\mathbf{v}_c \cdot \mathbf{n}] = 0, \quad (9)$$

which implies

$$[\mu \nabla P_c \cdot \mathbf{n}] = [\chi_E \nabla E \cdot \mathbf{n}], \quad (10)$$

where $\mathbf{n}$ is the unit outward normal to Σ. The velocity of the tumor-host interface is

$$V = -\mu \nabla P_c \cdot \mathbf{n} + \chi_E \nabla E \cdot \mathbf{n}. \quad (11)$$

In the far-field, the pressure is assumed to satisfy no-flux boundary conditions $P_c / n = 0$.

2.1.3 Model of IFP and IFF—We assume the water and cell volume fractions are φ_f and φ_c, respectively, where

$$\varphi_f + \varphi_c = 1. \quad (12)$$

For simplicity, we assume that φ_f and φ_c are constants. We further assume that the liquid and solid phases have equal densities. Appealing to mass conservation, we have:

$$\nabla \cdot (\varphi_f \mathbf{v_f}) + \nabla \cdot (\varphi_c \mathbf{v_c}) = S_V + S_L \quad (13)$$

where $\mathbf{v}_f$ and $\mathbf{v_c}$ are the IFF and cell velocity, respectively, and S_V represents the source of interstitial fluid from the vasculature and S_L represents the sink of interstitial fluid into the lymphatic network. The term S_V is taken to be

$$S_V = \lambda_{Vf} \cdot (P_e - P_f) \cdot 1_{vessel}, \quad (14)$$

where λ_{Vf} is the fluid exchange rate from vessels and P_e is an effective pressure (defined below). We may relate λ_{Vf} to the vessel surface area per unit volume V_T for transport in the interstitium as $\lambda_{Vf} = \dfrac{K_{Vf} S_A}{V_T}$.

The effective pressure P_e is defined as the IFP value that yields zero net volume flux out of the vasculature (Baxter & Jain, 1989), and is given by

$$P_e = P_v - \omega(\pi_v - \pi_i), \quad (15)$$

where the blood vessel pressure P_v is computed from the vasculature flow (see Eq. (24) below), ω is the average osmotic reflection coefficient for plasma proteins, π_v is the osmotic pressure of the plasma and π_i is the osmotic pressure of the interstitial fluid.

We model the lymphatics by a continuous density field L. We assume that the fluid drainage capacity in the interstitium is proportional to the local lymphatic density, that the lymphatic density is decreased by the action of matrix degrading enzymes and that drainage can also be regulated by the tumor stress-induced collapse of lymphatic vessels. We further assume there is no flow from the lymphatic system into the interstitium. Therefore, the drainage by the lymphatic system is modeled as:

$$S_L = -\lambda_{fL} c(P_c, L)(P_f - P_L) \cdot 1_{P_f > P_L}, \quad (16)$$

where $1_{P_f > P_L}$ is a volume indicator function, and $c(P_c, L)$ is regulated by the tumor hydrostatic pressure and lymphatic density:

$$c(P_c, L) = \begin{cases} (1 + \frac{Lymmax - 1}{KLmin} P_c)L & P_c \leq KL_{min} \\ Lymmax(1 - \frac{P_c - KL_{min}}{KL_{max} - KL_{min}})L & KL_{min} < P_c \leq KL_{max} \\ 0 & P_c > KL_{max} \end{cases} \quad (17)$$

where KL_{min} and KL_{max} are partial collapse thresholds. For small hydrostatic pressures P below the partial collapse threshold KL_{min}, $c(P, L)$ increases with P and the drainage increases as pressure from the cells pushes fluid into the lymphatic vessels ($Lymmax \times L$ at the maximum). When the pressure increases beyond KL_{min}, the lymphatic vessels begin to partially close and $c(P, L)$ subsequently decreases and reaches 0 at and beyond KL_{max} where the lymphatic vessels collapse. Also, we assume the continuous lymphatic vessel field is degraded by the matrix degrading enzyme, M (described in the Appendix) at rate λ_{ML}, thus

$$\frac{dL}{dt} = -\lambda_{ML} ML. \quad (18)$$

Simultaneously, we have for the cell velocity derived from Eq.5:

$$\nabla \cdot (\varphi_c \mathbf{v_c}) = \varphi_c \lambda_M \lambda_p(\sigma) \quad (19)$$

where λ_M is the rate of mitosis/apoptosis. Cell death thus provides a fluid source while proliferation provides a sink. By Darcy's law, $\mathbf{v_f} = -K\nabla P_f$ and combining Eqs. (13)–(19), we have:

$$\nabla \cdot (-\varphi_f K\nabla P_f) = \lambda_{Vf}(P_e - P_f) \cdot 1_{P_e > P_f} - \lambda_{fL} c(P, L)(P_f - P_L) \cdot 1_{P_f > P_L} - \varphi_c \lambda_M \lambda_p(\sigma). \quad (20)$$

for the IFP, where drainage occurs when P_f exceeds the effective lymphatic drainage pressure P_L.

Interestingly, from Eq.20 we can demonstrate that the average tumor IFP becomes insensitive to lymphatic drainage as the vascular hydraulic conductivity increases. Let us simplify Eq. (20) by eliminating the cell uptake $\varphi_c \lambda_M \lambda_p(\sigma)$, the constraint $1_{P_e > P_f}$ and $1_{P_f > P_L}$. Then, integrating the result over the computational domain we obtain $\int_\omega \lambda_{Vf}(P_e - P_f) \, dx + \int_{\omega_c} \lambda_V(P_e - P_f) \, dx = \int_{\omega_L} \lambda_{fL} c(P, L)(P_f - P_L) \, dx$, using the Neumann boundary condition (which is the case for all our studies) where Ω_L is the functional region of lymphatics. If we further simplify the equation by assuming the $\lambda_{Vf} = \lambda_{VT}$, where λ_{VT} is a constant fluid extravasation rate in the tumor region Ω and models the product of the vascular hydraulic conductivity and tumor vascular surface area per volume, we obtain

$\frac{1}{s_\Omega} \int_\Omega P_f \, dx = \frac{1}{s_\Omega} \int_\Omega P_e \, dx + \frac{1}{\lambda_{VT} s_\Omega}(\int_{\Omega^c} \lambda_{Vf}(P_e - P_f) \, dx - \int_{\Omega_L} \lambda_{fL} c(P, L)(P_f - P_L)) \, dx$. This formula shows that increasing λ_{VT} in the tumor decreases the sensitivity of the average tumor IFP to the lymphatic drainage. We also conclude that average P_f in tumor is at least linearly dependent on the average tumor P_e, which increases where the osmotic pressure difference decreases. We also show in Sec. 4.4 that the spatial distribution of IFP is insensitive to the lymphatic parameters as the vascular hydraulic conductivity increases.

2.2 Angiogenesis and blood flow in the capillary network

Following (McDougall *et al.*, 2002; McDougall *et al.*, 2006), we define the vasculature on a Cartesian grid. A vessel node is the basic unit located at a grid point and the vasculature configuration is given by the connection between neighbouring nodes. Responding to the

TAF released by the hypoxic cells in the tumor, endothelial cell sprouts are generated, grow and fuse to expand the vascular network. red In previous work (Macklin *et al.*, 2009), the pre-existing vasculature is described as a continuous vessel density field and an explicit parent vessel lying at one of the boundaries. New and pre-existing vessels are insulated from each other: New sprouts can be generated from the explicit parent vessel or its descendent and they are unable to anastomosis with the pre-existing vessels. Here we describe the pre-existing vasculature as grid-like network where sprouts can be generated from and fuse into, analogous to (Bartha & Rieger, 2006; Lee *et al.*, 2006a; Welter *et al.*, 2008; Welter *et al.*, 2009; Welter *et al.*, 2010).

During angiogenesis, the sprouting pattern along stimulated vessels can be mediated by Notch-Delta signaling between adjacent endothelial cells (ECs) that ensures no adjacent ECs sprout simultaneously under the influence of TAF (Williams *et al.*, 2006; Hellström *et al.*, 2007; Jakobsson *et al.*, 2009). A theoretical study focusing on the details of lateral inhibition was performed by (Bentley *et al.*, 2008) and the resulting pattern is considered in (Welter *et al.*, 2009). Here we also incorporate this sprout generating pattern. After sprouts are generated, they advance according to TAF and ECM gradient stochastically following (McDougall *et al.*, 2002; McDougall *et al.*, 2006; Macklin *et al.*, 2009). In the developing capillary network, blood begins to flow and the blood vessel pressure and flow are computed along the vessels. The vessel radius is adapted to the local vessel pressure, shear rate and metabolite level following (Pries *et al.*, 1998). In (McDougall *et al.*, 2002; McDougall *et al.*, 2006), the vasculature is assumed to consist of cylindrical segments connected at vessel nodes and obeying fluid conservation with no fluid extravasation due to vessel leakiness taken into consideration. The flow rate Q_{qp} from two connected vessel nodes q to p can be determined from a Poiseuille-like model (Fung, 1997):

$$Q_{qp} = \frac{\pi R_{pq}^4 (P_{v_q} - P_{v_p})}{8 \mu_{apparent} L} \quad (21)$$

where P_{v_p} and P_{v_q} are the corresponding blood pressures, R_{pq} is the radius of the vessel segment from q to p, the apparent viscosity $\mu_{apparent} = \mu_{plasma} \cdot \mu_{rel}$ where μ_{plasma} is the plasma viscosity and μ_{ref} is the relative viscosity as a function of blood hematocrit and vessel radius (Pries *et al.*, 1998).

In this paper, we consider flow conservation in the presence of transcapillary fluid flux. Thus, for each node p:

$$\sum_q Q_{qp} = O_V \quad (22)$$

where q represents all the neighboring nodes and

$$O_V = K_{Vf} S_V (P_e - P_f) \quad (23)$$

is the fluid extravasation rate at node p into the interstitium.

Coupling the flux of fluid into the interstitium with the blood flow, we solve the blood vessel pressure P_V along the vessel network by:

$$K_{Vf} S_V (P_e - P_f) = \sum_q \frac{\pi R_{pq}^4 (P_{v_q} - P_{v_p})}{8 \mu_{apparent} L}. \quad (24)$$

2.3 Stimuli influencing vessel radius adaptation

Following (Pries *et al.*, 1998; McDougall *et al.*, 2002; McDougall *et al.*, 2006; Macklin *et al.*, 2009), the vessel radii are adapted in response to wall shear stress, intravascular pressure and hematocrit. Accordingly, the change in radius ΔR over a time unit is given by:

$$\Delta R = (S_{wss} + S_p + S_m - S_s)\, R\Delta t, \quad (25)$$

$$S_{wss} = \log(\tau_\omega + \tau_{ref}), \quad (26)$$

$$S_p = -k_p \log \tau_e(P_v), \quad (27)$$

$$S_m = k_m \log\left(\frac{Q_{ref}}{QH_D} + 1\right), \quad (28)$$

where S_{wss} is the stimulus from wall shear stress τ_ω, and τ_{ref} is a constant included to avoid singular behavior at low shear rates. The wall shear stress τ_ω is calculated from (Pries *et al.*, 1998; Pries *et al.*, 1992):

$$\tau_\omega = \frac{4\mu_{app}(R, H_D)}{\pi R^3} |Q| \quad (29)$$

where μ_{app} is apparent viscosity and can be computed as a function of vessel radius and hematocrit (see the previous references). The term $|Q|$ is the absolute value of the flow rate, which will be specified numerically later. Further, S_p is the stimulus by the intravascular pressure (considering only the vessel pressure) in the form of $\tau_e(P_v)$ from:

$$\tau_e(P_v) = 100 - 86 \cdot \exp\left[-5000 \cdot [\log(\log P_v)]^{5.4}\right], \quad (30)$$

where the values are obtained from (Pries *et al.*, 1998; McDougall *et al.*, 2002; McDougall *et al.*, 2006; Macklin *et al.*, 2009). Finally, S_m is the stimulus from the flow carrying hematocrit, where Q_{ref} is a reference flow rate that is assumed to be larger than most of the flows in the network. The parameters k_p and k_m are the intensity coefficients. red We are aware vessel dilation by circumferential growth as a result of endothelial cell proliferation may be dominant inside the tumor (Erber *et al.*, 2006; Holash *et al.*, 1999*a*). This was implemented in (Bartha & Rieger, 2006; Lee *et al.*, 2006*a*; Welter *et al.*, 2008; Welter *et al.*, 2009; Welter *et al.*, 2010) but this is beyond the scope of this paper, where we emphasize the effect of solid tumor pressure. We will investigate circumferential growth in a future work.

2.3.1 Hydrostatic-induced vessel collapse—red Cancer cells are known to compress intratumor vessels, which may result in a decrease in effective vessel radii that may recover after the excessive stress by cell proliferation is removed (Padera *et al.*, 2004). In the radius adaptation model used in (Pries *et al.*, 2010), the shrinking tendency S_s is set to a constant $S_s = k_s$, where k_s is the tendency to shrink. Here, however, we couple the vascular collapse due to the tumor pressure into S_s to obtain:

$$S_s = S_{pc} = \begin{cases} k_s & P_c \leq P_{CT} \\ k_s + k_{pc}(P_c - P_{CT}) & P_c > P_{CT} \end{cases} \quad (31)$$

When the tumor pressure P_c is smaller than the pressure-sensing level P_{CT}, the formula is the same as the original version. When the pressure increases beyond P_{CT}, the shrinking tendency is assumed to increase with P_c at rate k_{pc}. red This may result in a vanishing effective radius representing vessels that have entirely collapsed. This may in turn be followed by partial recovery if the stress is relieved. Implementation details are in Sec.3.2.2. We are aware of the important role of wall shear stress on vessel wall degradation and collapse (Holash *et al.*, 1999*a*), which is due to poor circulation in the vascular network following tumor-pressure induced vessel collapse. Using an ad-hoc model for tumor pressure, (Bartha & Rieger, 2006; Lee *et al.*, 2006*a*; Welter *et al.*, 2008; Welter *et al.*, 2009; Welter *et al.*, 2010) previously considered the effects of wall shear stress on vessel collapse. We will model this effect in a future work.

3 Numerical details

3.1 The coupling of variables in the continuous field

To solve for the oxygen concentration, tumor pressure, IFP and other diffusible chemical factors (*MDE* and *TAF*), we discretize the corresponding elliptic/parabolic equations (1), (4), (20), (32) and (34) in space using centered finite difference approximations and the backward Euler time-stepping algorithm. The discrete equations are then solved using a nonlinear adaptive Gauss-Seidel iterative method (NAGSI)(Macklin & Lowengrub, 2007; Macklin & Lowengrub, 2008). The ghost cell method developed in (Macklin & Lowengrub, 2008) is used to implement the tumor pressure jump condition at the interface in Eq.(8). In previous work (Macklin *et al.*, 2009), each equation was solved separately by lagging the source terms. We found that this could lead to non-biophysical oscillations of the fields in time and space. We eliminate this behavior by iteratively solving the system of equations for the oxygen concentration, tumor pressure, IFP and blood vessel pressure together to steady state at each time step, e.g., the system of equations is discretized implicitly in time. The hematocrit level is computed once every few iterations, which is affected by the blood flow and in turn influences the oxygen extravasation. Note that the vessel radii, however, are still discretized explicitly. We use the level set method to update the tumor viable/necrotic region, the tumor-host interface and the viable-necrotic interface. Further details on the numerical implementation can be found in (Macklin *et al.*, 2009) and the references therein.

3.2 Angiogenesis model

The Cartesian mesh for the tumor growth system coincides with that used for the vessel network. redFor a fixed tumor geometry and *TAF* distribution, the vascular network is grown using the same time steps as the tumor. The sprout generation process is described in Sec. 3.2.1 and the movement of sprouts is according to (Anderson & Chaplain, 1998; Stephanou *et al.*, 2005; Chaplain, 1995). After each update of the network, the blood pressure and flow in Eq. (24) are solved together with the IFP, oxygen, and pressure to the steady state. Then the vessel radius is updated explicitly using the same time steps as the tumor growth. red

3.2.1 Contact units and sprout generation—A contact unit consists of a group of vessel nodes connected with cylindrical segments; here 15 nodes are used. If a vessel node within a contact unit has a TAF level beyond a stimulating threshold, the contact unit becomes activated. Activated contact units compete along the vessel as described below. We put all activated contact unit candidates into set $\Omega_{S \cup T}$; then we do the following:

- From $\Omega_{S \cup T}$, we mark contact units with higher level of TAF than their immediate neighbors along the vasculature as the first population of tip generating units T_1 and mark their neighbors as S_1.

- If $\Omega_{S \cup T} \backslash S_1 \backslash T_1$ is not empty, we mark another population of the tip generating units and neighboring units in the same way as the previous step.

- Repeat the above until the set $\Omega_{S \cup T} \backslash (\overset{n}{\underset{i=1}{\cup}} S_i) \backslash (\overset{n}{\underset{i=1}{\cup}} T_i)$ becomes empty.

Then $\overset{n}{\underset{i=1}{\cup}} T_i$ are the tip generating units and $\overset{n}{\underset{i=1}{\cup}} S_i$ are the neighboring non-tip units, out of all the activated candidates. We generate sprouting or branching nodes in each tip generating units by choosing the one with maximal TAF level within the unit. A contact unit can have at most only one sprouting node. In this way, we avoid the generation of two or more branches within a short distance, and we model the result of Notch-Delta signaling and lateral inhibition (Bentley *et al.*, 2008).

3.2.2 Radius collapsing selection—The update of the vessel radius follows the methods in (Pries *et al.*, 1998; McDougall *et al.*, 2002; Macklin *et al.*, 2009), after which the vessels are evaluated for possible collapse if the radius R has become too small (e.g., $R < R_{min}$, where $R_{min} = 2e - 6m$). For each vessel segment,

- if the radius R is equal to or larger than R_{min}, the vessel radius is updated via Eq. (25).

- if R is smaller than R_{min} and $P < P_{CT}$, set $R = R_{min}$ and remain adapting according to Eq. 25. This simulates the case of a vessel that was collapsing but the pressure has been relieved.

- if R is smaller than R_{min} and $P > P_{CT}$, set $R = 0$ and stop adapting. This simulates the case of a vessel that has now collapsed due to the pressure.

- if R is 0 and $P < P_{CT}$, then set $R = R_{min}$ and begin adaptation. This simulates the case of a vessel that was collapsed, but the pressure has decreased to the point that minimum flow can occur.

- if R is 0 and $P > P_{CT}$, maintain $R = 0$. This simulates a collapsed vessel remaining collapsed due to the high pressure.

- if the blood vessel pressure P_v is computed to be 0 due to the collapsing of all the connected vessels, set $R = 0$. This simulates the collapse of a whole group of vessels for which the flow has stopped.

3.3 Overall Computational Solution Technique

1. At each time step, iteratively solve Eqs.(1), (4), (20) and (24) together for the oxygen concentration, tumor pressure, IFP and blood vessel pressure. At each iteration, pressure and oxygen are implicitly solved and the position of the hypoxic region is updated until all variables converge. The hypoxic region is identified by: $\Omega_H = \{\mathbf{x} : \sigma(\mathbf{x}, t) < \sigma_H\} \cap \Omega$. The hematocrit level is updated every 500 iterations. With this number of iterations, the hematocrit level was found to be consistent with physiological conditions. We then use the solution σ to update the position of the necrotic core: $\Omega_N^{updated} = \Omega_N^{previous} \cup (\{\mathbf{x} : \sigma(\mathbf{x}, t) < \sigma_N\} \cap \Omega)$. We then rebuild φ_N, a level set function, that represents the updated region Ω_N (Macklin *et al.*, 2009), and update the position of the tumor/host interface Σ and the necrotic/viable Σ_N by advecting the level set functions φ and φ_N.

2. Solve Eq.(34) for the TAF concentration using the updated hypoxic region Ω_H from step 1 and update the MDE concentration and ECM density according to Eqs. (32) and (33).

3. Update the vessel radius and the collapsing selection according to Eqs.(25) and the algorithm described in Sec. 3.2.2.

4. Using the updated tumor position in step 1, and the TAF, MDE and ECM obtained in step 2, grow the vasculature and go back to step 1.

4 Simulation and Parameter Studies

We begin by presenting a simulation of vascular tumor growth under the effect of blood/ lymphatic vessels fluid extravasation/drainage with the parameters listed in Table 1 for the lymphatics, Table 2 for the discrete vasculature and Table 3 in the Appendix for the tumor model in which the parameters are as in (Macklin *et al.*, 2009). At first, oxygen extravasation is not affected by IFP (k_{P_f} = 0). Then, we consider the effects of IFP on oxygen extravasation (k_{P_f} > 0), and discuss the effects of lymphatic/blood vessel collapse on the tumor growth. Finally, we discuss the role of elevated vascular/interstitial hydraulic conductivities and attenuated osmotic pressure differences on the interstitial fluid dynamics and vascular tumor growth.

4.1 Initialization of the tumor and vascular network

The simulations are performed on a $2 \times 2mm^2$ area with a uniform pre-existing vascular network arranged on a Cartesian grid (Fig. 2)red, which was also done in (Bartha & Rieger, 2006). We impose a pressure gradient on the boundary of the domain starting with 3750 Pa.s at the lower left and with the pressure at the upper right equal to 3000 Pa.s with linear pressure decrements in between. Thus the 16 vessel nodes along the left and bottom boundaries are inlets while the other 16 vessel nodes along the right and top boundaries outlets. We then calibrate the model such that the vasculature provides sufficient oxygen (σ = 0.76 ~ 1) to support normal tissue metabolism (Intaglietta *et al.*, 1996). A small avascular (Fig. 2) tumor is then placed at the center of the domain. Since the tumor consumes more oxygen than the surrounding tissue, the oxygen level in the tumor region is smaller. As the tumor grows, the oxygen concentration in the tumor interior decreases and cells become hypoxic (blue) and necrotic (brown), see Figs. (3 – 6).

4.2 Simulation of tumor growth and IFP

In Figs. 2–6, we present the evolution of a vascular tumor and the vascular network when the vessels are leaky and the lymphatic vessels are functional. In this simulation, k_{P_f} = 0, so that IFP does not affect oxygen extravasation. At early times (t = 1.5 days), vessel sprouts form but there is very little functional neovasculature, and all the extravasating fluid (and the drainage by the lymphatic system) is localized around the pre-existing vasculature. At later times, tumor growth and angiogenesis continue and the neovasculature is more functional (Figs. 3–6). The IFP in the tumor is now elevated because of fluid extravasation from the neovasculature and the pressure-induced collapse of the lymphatic network by proliferating tumor cells. Accordingly, there is little lymphatic drainage in the tumor interior. The drainage instead occurs a small distance from the tumor margin. The oxygen, vessel pressure and TAF distributions become progressively more heterogeneous as a result of the interplay between tumor growth and the vascular response. Oxygen is elevated outside the tumor as well as in certain regions inside where there are newly formed functional vessels. The heterogeneous oxygen distribution leads to heterogeneous distributions of hypoxic and necrotic cells, which in turn leads to a heterogeneous distribution of TAF and vessel sprouts. The vessel pressure generally is high in the lower left and low at the upper right, due to the imposed inflow/outflow boundary conditions. By day 18, the tumor is approximately 1.5 mm in diameter. As the tumor grows, the IFP increases significantly reflecting the inhibited drainage of the interstitial fluid by the pressure-induced lymphatic collapse, which extends further into the host tissue with little drainage. The IFP inside the region where there is little

drainage results in outward flow of interstitial fluid flow into regions of the host tissue with more functional lymphatics and better drainage. Figs. 7 and 8 show the tumor cell velocity and interstitial fluid velocity which are both directed from the tumor to the host tissue. The interstitial fluid velocity is particularly large at the tumor boundary.

When IFP inhibits oxygen extravasation, the tumor growth and the host vascular response is qualitatively similar, although the tumor grows more slowly. Compare the middle column of Fig. 13, where $k_{P_f} = 0.5$, with Fig. 6.

4.3 Vessel resistance, IFP and tumor growth

Next, we vary the blood/lymphatic vessel resistance to the hydrostatic pressure and quantify the consequences on IFP and tumor growth.

4.3.1 Resistance of blood vessels to hydrostatic pressure—In Figs. 9 and 10, we present an evolution sequence ($t = 12, 18$) of vascular tumor growth and host angiogenic response, for a moderate level of vessel resistance $P_{CT} = 2.0$. The lymphatic vessels are assumed to be fully functional $c(P_c, L) = 1$. The other parameters correspond to those used in Figs. 2–6. The hydrostatic pressure induces blood vessel collapse, and leads to heterogeneous delivery of oxygen in the tumor microenvironment. The collapse is mainly confined to the tumor interior at early times, while vessels in the tumor microenvironment collapse at later times. The blue and red ovals denote regions where significant numbers of vessels have collapsed (e.g., having zero radius). In addition, vessel collapse also induces a loss of functionality of vessels downstream of the collapsed vessels until the network is able to re-organize. Because the lymphatic drainage is unimpaired by the hydrostatic pressure, the IFP is significantly smaller than that in Figs. 6. In Fig. 11, we compare the results using less resistant blood vessels ($P_{CT} = 1.0$, left column) and more resistant blood vessels ($P_{CT} = 3.0$, right column). The center column corresponds to the result from Fig. 10.

Because vessel collapse reduces oxygen and nutrient transport to the tumor microenvironment, the tumor size increases as P_{CT} increases and the vessels become more structurally sound. This is quantified in Fig. 12 where the equivalent radius (radius of circle with the same enclosed area) of the tumors are plotted. Note that the change in radius tends to become linear in time as the tumor grows red since proliferation is confined to the tumor boundary, in agreement with recent experimental results (Lee *et al.*, 2006*b*) and theoretical predictions (Alvord Jr, 1977; Cristini *et al.*, 2003; Brú *et al.*, 1998; Brú *et al.*, 2003; Bartha & Rieger, 2006; Lee *et al.*, 2006*a*; Welter *et al.*, 2008; Welter *et al.*, 2009; Welter *et al.*, 2010). In addition, the hydrostatic pressure also increases as a function of P_{CT} due to enhanced proliferation. Accordingly, we find that the maximum hydrostatic pressure also increases with P_{CT}.

4.3.2 Resistance of lymphatic vessels to hydrostatic pressure—We next investigate the effects of lymphatic vessel resistance to the hydrostatic pressure by varying the parameter KL_{max} in Eq. (17). The results are presented in Figs. 13–15. A large region develops when the lymphatics are easily collapsed, and extends well beyond the tumor into the host where there is no drainage of interstitial fluid (Fig. 13, left column). Accordingly, the region where the IFP is high is also high, which impairs the extravasation of oxygen. See (Fig. 14) as well, which shows the average IFP in the tumor. This in turn impedes the growth of the tumor and leads to a large fraction of the tumor to become hypoxic and necrotic (Fig. 15 shows the equivalent tumor radius as a function of time). As KL_{max} is increased, the lymphatic vessels are more resistant to collapse and as a consequence, there is more fluid drainage, oxygen delivery and tumor growth, as seen in Fig. 14 at late times. At early times, the growth is more strongly influenced by stochastic variations in the vascular

structure (e.g., different realizations show different ordering in the tumor radii as a function of *KLmax* at early times $t \lesssim 10$).

4.3.3 Resistance of both blood and lymphatic vessels to hydrostatic pressure

—We next consider the combined effects of blood and lymphatic vessel collapse. Unlike the simulations shown in Figs. 9 – 12, the lymphatic vessels may now collapse. In particular, we fix KL_{max} and vary P_{CT}. The results are presented in Figs. 16 and 17 which show the evolution of the average IFP and the equivalent tumor radius, respectively. As P_{CT} increases, the IFP also increases because the blood vessels resist collapse and thus are better able to extravasate liquid. However, the effect seems to saturate due to the feedback between IFP, oxygen extravasation, lymphatic drainage, and tumor growth. For example, oxygen extravasation is reduced as IFP increases, which results in less proliferation, less lymphatic vessel collapse and better drainage of interstitial fluid. As P_{CT} increases beyond a critical threshold, these processes begin to balance one another. The oscillation in the curves for P_{CT} = 1 and P_{CT} = 2 results from the vessel recovery and collapse, and is an artifact of the simulation by not solving this part of the system implicitly. For the case P_{CT} = 3, no blood vessels collapse since the tumor pressure P_c never exceeds 3 because the IFP impedes nutrient extravasation and tumor cell proliferation.

4.4 The effect of tumor vascular pathologies

It is known experimentally that vascular hydraulic conductivity λ_{Vf} may result from weakened junctions between vascular endothelial cells, which can be caused by increased VEGF concentrations (e.g., (Gavard & Gutkind, 2006)) as well as decreases in the number of pericyte and smooth muscle cells surrounding the vessels (e.g., (Daneman *et al.*, 2010)). In addition, the interstitial hydraulic conductivity K_i in the tumor may also be elevated if the tumor extracellular matrix (ECM) density is smaller than that in the host (e.g., (Levick, 1987)). Finally, an accumulation of plasma proteins in the tumor tissue due to poorly functioning lymphatics and an elevated vascular hydraulic conductivity may lead to a decrease in the osmotic pressure difference across blood vessel walls $\omega(\pi_v - \pi_i)$ (e.g., (Burgen & Francombe, 1962; Baxter & Jain, 1989)). We explore these pathological effects on the IFP distribution while at the same time varying the lymphatic collapsing threshold. To best illustrate the effects, we fix the tumor morphology and the vascular network.

As a control, we consider a case in which the host and tumor regions share the same interstitial hydraulic conductivity K_i, vascular hydraulic conductivity λ_{Vf} and osmotic pressure difference $\omega(\pi_v - \pi_i)$, but the lymphatic collapse threshold KL_{max} is varied. The result is shown in Fig. 18, where it is seen that a smaller lymphatic collapsing threshold KL_{max} contributes to a larger drainage-free zone for the same tumor and vasculature configurations.

We now explore and compare individual pathological effects under different lymphatic vessel distributions. We plot the IFP through the tumor center. In Fig. 19, the red curve is the IFP distribution and the red curve in Fig. 20 is the IFP gradient in the tumor directed outward $\nabla P_i \cdot \mathbf{n}_{out}$, where $\mathbf{n}_{out}$ is the outward normal vector, and which corresponds to the outward speed of the fluid in the control tumor in Fig. 18. The brown curve corresponds to the situation where $\omega(\pi_v - \pi_i)$ is smaller in the tumor than the host. The green and blue curves correspond to the cases where λ_{Vf} and K_i in the tumor are larger than that in the host, respectively. In each case, a smaller lymphatic collapsing threshold contributes to higher IFP (Fig. 19) red and the IFP gradient $\nabla P_i \cdot \mathbf{n}_{out}$ spikes farther from the tumor center (Fig. 20). The diminished osmotic pressure difference (brown curves in Fig. 19) contributes to higher IFP while the IFP is sensitive to different lymphatic distributions. Elevated vascular hydraulic conductivity in the tumor (green curves in Fig. 19) also contributes to

higher IFP but is fairly insensitive to different lymphatic distributions, as suggested by the analysis in Sec. 2.1.3. This enables the tumor to maintain a hypertension profile under variations of the lymphatic system. Elevated tumor interstitial hydraulic conductivity (blue curves in Fig. 19) flattens the IFP distribution and contributes to a plateau profile in the tumor when the lymphatics collapse easily (the blue curve when $KL_{max} = 1$ in Fig. 19). red Except for the cases with attenuated osmotic pressure difference (brown), all the other cases exhibit tumor IFP values lying in the range of experimentally measured values (1000–2000 *Pa*, (Boucher *et al.*, 1990)). The inconsistency with experimentally observed IFP when there is an attenuated osmotic pressure difference is likely due to the large imposed pressure distribution (3000–3750 *Pa*) on the boundary of the domain.

In Fig. 21 we quantify the average IFF red velocities leaving the tumor, either to the tumor lymphatics (left) or the host tissue (right) versus *KLmax*. This gives insight into how variation in lymphatic resistance may affect tumor cell metastasis under various pathological conditions. red We compute the average IFF velocity ($\mu m/s$) of fluid leaving through the tumor lymphatics by taking the total drainage in the tumor ($\mu m^3/s$) divided by the tumor area (μm^2). We compute the average velocity of fluid flowing into the host tissue by taking the total flow into the host (obtained as the net fluid extravasation in the tumor, subtracting the amount drained by the lymphatics, which has units $\mu m^3/s$), divided by the effective tumor boundary (obtained by $2\sqrt{\pi Tumor\,Area}\sqrt[3]{V_T}$, which has units μm^2. Note that V_T is the characteristic volume of the tumor– see Table 1). The largest red velocities of IFF leaving the red tumor into the host tissue (right panel) occur when all pathologies are included (attenuated osmotic pressure differences, elevated vascular and interstitial hydraulic conductivities; cyan), followed by the case in which both the vascular and interstitial hydraulic conductivities are elevated (black). The green curve denotes the case in which only the vascular hydraulic conductivity is elevated, while the brown, blue and red curves mark the cases with attenuated osmotic pressure differences, elevated interstitial hydraulic conductivity and the control, respectively. red The IFF velocity at the tumor boundary was reported in the order of 0.1μ m/s from experimental measurements (Jain, 1987*b*), which is satisfied when *KLmax* 2 with elevated vascular hydraulic conductivities (cyan, black and green). Further, the red increase of the IFF velocity into the host tissue saturates because the IFP (and IFF) saturates as *KLmax* increases (recall Figs. 19 and 20) while red the IFF velocity into the lymphatics continues to increase (left panel) since the lymphatic vessels are more resistant to collapse as *KLmax* increases. Note that when red*KLmax* < 2, all the lymphatic vessels in the tumor are collapsed so that the rate of IFF removal to the lymphatics is zero. Thus for all cases the IFF is solely directed into the host tissue when red *KLmax* < 2. When the interstitial hydraulic conductivity is elevated (blue), observe that red almost all the interstitial fluid leaves the tumor through the tissue and not through the lymphatics for all *KLmax*. This is because when the interstitial hydraulic conductivity is elevated, the IFP distribution is flatter and broader than the other cases (recall Fig. 19) and thus elevated hydraulic conductivity contributes to a more uniform regulating effect on oxygen extravasation. This in turn makes the hydrostatic tumor pressure distribution more uniform and collapses more tumor lymphatic vessels compared to the other three cases (red, brown and green) with the same lymphatic resistance, even though the maximum IFP is lower than those cases (red, brown, green) when the interstitial hydraulic conductivity is elevated (Fig. 19). red This is consistent with the behavior observed when there is elevated vascular hydraulic conductivity.

5 Discussion

We have extended previous vascular tumor modeling work by accounting for interstitial fluid pressure (IFP) and flow (IFF) as well as drainage by lymphatic vessels. We have considered blood flow with leaky vessels and have coupled the transcapillary flux with IFP.

In contrast with previous work where oxygen extravasation was directly regulated by the tumor hydrostatic pressure, here regulation occurs via IFP and the hydrostatic pressure indirectly regulates extravasation by contributing to the collapse of both lymphatic and blood vessels. We have also replaced the continuous pre-existing vessel field in previous tumor modeling work by a discrete vascular network, which is the sole source of oxygen extravasation. In this way, the coupling between discrete angiogenesis and the continuous tumor model via oxygen is more absolute. To solve the system numerically, we develop a fully implicit discretization, which eliminates the occurance of non-biophysical oscillations of the fields in time and space when each equation were to be solved separately by lagging the source terms (as was done in previous work (Macklin *et al.*, 2009)).

In agreement with experimental observations, tumor pressure-induced blood vessel collapse is seen to contribute to hypoxia and necrosis while the pressure-induced collapse of lymphatic vessels contributes to large IFP and large IFF directed towards the host tissue, both of which contribute barriers to transport of oxygen, nutrients and potentially chemotherapy agents to the tumor. The effect of tumor pressure is not localized - vessels can be forced to collapse if they become fully deprived of blood flow due to the collapse of vessels upstream. Also, neighboring vessels and those downstream of collapsed vessels may be partially deprived of blood flow due to changes in the flow network.

We also investigated the effect of tumor vascular pathologies, including elevated vascular and interstitial hydraulic conductivities inside the tumor as well as diminished osmotic pressure differences, on the fluid flow across the tumor capillary bed, the lymphatic drainage, and the IFP. We identified a combination of tumor lymphatic conditions and elevated interstitial hydraulic conductivity that contributes to a plateau of the IFP across the tumor and a collapse of tumor lymphatic vessels, both of which are observed in experiments (e.g., (Boucher *et al.*, 1990)). In particular, our results revealed that elevated interstitial hydraulic conductivity together with poor lymphatic function is the root cause of the plateau profile, which expands upon earlier work by (Baxter & Jain, 1989) who considered all the pathologies simultaneously in the context of a simpler model. Thus, our model suggests the following testable prediction: If the tumor IFP exhibits a plateau, then the interstitial hydraulic conductivity in the tumor is elevated. Taking this together with experimental data that correlates increased tumor interstitial hydraulic conductivities with decreased ECM densities in the tumor (Levick, 1987), we predict that if the tumor ECM density is smaller than that in the host tissue (which can be assessed non-invasively), then the tumor IFP exhibits a plateau, which makes the tumor hydrostatic pressure more uniform and results in strong vascular and interstitial fluid transport barriers to the tumor that, in the absence of other effects, suggests that standard chemotherapy would be less effective than might otherwise be the case. A more complete description of transport barriers should also take into account the binding of drugs to the ECM (Brown *et al.*, 2003; Minchinton & Tannock, 2006; Tredan *et al.*, 2007), this will be considered in a future work.

It has been reported that interstitial fluid flow contributes to tumor invasion and metastasis directly through *CCR*7 signaling (Shields *et al.*, 2007; Shieh & Swartz, 2011). In particular, tumor cells chemotax up gradients of *CCR*7 ligands, which are released into the interstitial fluid by lymphatic endothelial cells and tumor cells themselves. We have found that the rate that IFF is fluxed into the lymphatics and host tissue is largely controlled by an elevated vascular hydraulic conductivity in the tumor. This provides another testable model prediction: tumors with increased vascular hydraulic conductivity (which could be measured non-invasively) are more likely to be locally invasive and to metastasize via the lymph system than those without. We also find that when the tumor vascular hydraulic conductivity is increased relative to the host, the IFF and IFP spatial profiles in the tumor are largely insensitive to the lymphatic collapse parameter *KLmax*. This results in a non-monotone

dependence of the IFF on *KLmax* as described in Sec. 4.4. In particular, taking *KLmax* large, which increases the resistance of the lymphatic vessels to collapse, actually decreases the rate of IFF into the host tissue and with it the risk of local invasion. Instead, it is more likely that invasion/metastasis occurs through drainage into the lymphatic system. Thus, our results suggest the possibility of developing strategies of targeting tumor cells based on the cues in the interstitial fluid.

red In this study, we made several simple assumptions that each may lead to a more extensive investigation. First of all, we assume the IFP affects oxygen extravasation through the transvascular fluid flux, thus a higher IFP distribution hinders tumor growth in time by decreasing the oxygen transfer to the tissue (see Fig. 15). To our knowledge, there is no direct evidence that IFP is associated with oxygen extravasation but when the IFP and blood pressure are comparable, tumor cell hypoxia is increased and there is an unfavorable treatment response (Jain, 2005*a*). Note if there is no feedback from IFP on oxygen extravasation, then lymphatic resistance would not affect tumor growth as shown in Fig. 15 and tumors with elevated interstitial hydraulic conductivity alone would not collapse most of tumor lymphatic vessels since the oxygen extravasation would be more uniform. However, vascular pathologies also may be for responsible correlations between high IFP and insufficient oxygen delivery (Cai *et al.*, 2011). Future studies are needed to further elucidate the correlation between IFP and oxygen extravasation.

In this investigation, we have simplified the pre-existing vascular network to be a small patch of capillaries in an arteriole-venous vessel network. We modeled only the capillary portion of the network. The imposed blood pressure values at the 32 boundary vessel nodes as well as the host tissue osmotic pressure difference ensure there is no intravasation of fluid from the interstitium to the blood if there is no tumor, consistent with the modern experimental results which show that dynamically intravasation occurs rarely in the capillary portion of the network, except in the organs for fluid absorption functions (i.e., kidney, intestine and lymph nodes). See the review (Levick & Michel, 2010) for details. In future work, we will explicitly model the arteriole-venous vessel network, following methods developed in (Welter *et al.*, 2009).

Further, here we incorporated the vessel collapse by tumor stress (Padera *et al.*, 2004) using vessel radii adaption model by (Pries *et al.*, 1998). We explicitly connected tumor pressure with decreases of vessel radii and the eventual collapse, which creates an avascular region through excessive proliferation. The effect of tumor pressure is not localized - vessels can be forced to collapse if they become fully deprived of blood flow due to the collapsing of the upstream vessels, analogous to (Bartha & Rieger, 2006). Also, those neighboring and downstream vessels of the collapsed ones may be partially deprived of blood flow due to the change of the flow network. Note that the collapsed vessels in our simulations can be recovered as the tumor stress decreases followed by the neighboring vessels while they may undergo regression and contribute to irreversible vascular geometric remodeling (Bartha & Rieger, 2006; Welter *et al.*, 2009). In our model, we did not consider tumor vessel circumferential growth (Erber *et al.*, 2006). In future work, we will consider this effect following methods developed by (Bartha & Rieger, 2006; Welter *et al.*, 2009).

Acknowledgments

References

Alvord EC Jr. Growth rates of epidermoid tumors. Annals of Neurology. 1977; 2:367–370. [PubMed: 617575]

Anderson A, Chaplain M. Continuous and discrete mathematical model of tumour-induced angiogenesis. Bull Math Biol. 1998; 60:857–899. [PubMed: 9739618]

Anderson A, Quaranta V. Integrative mathematical oncology. Nature Reviews Cancer. 2008; 8:227–244.

Astanin, S.; Preziosi, L. Multiphase models of tumour growth. In: Bellomo, N.; Chaplain, M.; DeAngelis, E., editors. Selected Topics on Cancer Modelling: Genesis - Evolution - Immune Competition - Therapy. Birkhaeuser; Boston: 2007.

Bartha K, Rieger H. Vascular network remodeling via vessel cooption, regression and growth in tumors. Journal of Theoretical Biology. 2006; 241:903–918. [PubMed: 16545398]

Baxter LT, Jain RK. Transport of fluid and macromolecules in tumors i role of intersititial pressure and convection. Microvascular Research. 1989; 37:77–104. [PubMed: 2646512]

Bentley K, Gerhardt H, Bates P. Agent-based simulation of notch-mediated tip cell selection in angiogenic sprout initialisation. Journal of Theoretical Biology. 2008; 250:25–36. [PubMed: 18028963]

Boucher Y, Baxter L, Jain RK. Interstitial pressure gradients in tissue-isolated and subcutaneous tumors: implications for therapy. Cancer Research. 1990; 50:4478–4484. [PubMed: 2369726]

Brown E, McKee T, diTomaso E, Pluen A, Seed S, Boucher Y, Jain R. Dynamic imaging of collagen and its modulation in tumors in vivo using second-harmonic generation. Nature Med. 2003; 9:796–800. [PubMed: 12754503]

Brú A, Albertos S, Subiza JL, Garcia-Asenjo JL, Brú I. The universal dynamics of tumor growth. Biophysical Journal. 2003; 85:2948–2961. [PubMed: 14581197]

Brú A, Pastor JM, Fernaud I, Brú I, Melle S, Berenguer C. Super-rough dynamics on tumor growth. Physical Review Letters. 1998; 81:4008–4011.

Burgen ASV, Francombe WH. The role of plasma colloid osmotic pressure in the regulation of extracellular fluid. Proc Intern Union Physiol Sci. 1962; 2:130.

Byrne H. Dissecting cancer through mathematics: from the cell to the animal model. Nature Reviews Cancer. 2010; 10:221–230.

Cai Y, Xu S, Wu J, Long Q. Coupled modelling of tumour angiogenesis, tumour growth and blood perfusion. Journal of Theoretical Biology. 2011; 279:90–101. [PubMed: 21392511]

Chaplain M. The mathematical modelling of tumour angiogenesis and invasion. Acta Biotheor. 1995; 43:387–402. [PubMed: 8919350]

Cristini V, Lowengrub J, Nie Q. Nonlinear simulation of tumor growth. Journal of Mathematical Biology. 2003; 46:191–224. [PubMed: 12728333]

Daneman R, Zhou L, Kebede AA, Barres BA. Pericytes are required for blood–brain barrier integrity during embryogenesis. NATURE. 2010; 468:562–566. [PubMed: 20944625]

De Bock K, Cauwenberghs S, Carmeliet P. Vessel abnormalization: another hallmark of cancer? molecular mechanisms and therapeutic implications. Curr Opinion Gen Dev. 2011; 21:73–79.

Deisboeck TS, Couzin ID. Collective behavior in cancer cell populations. BioEssays. 2009; 31 (2):190–197. [PubMed: 19204991]

Endrich B, Reinhold H, Gross J, Intaglietta M. Tissue perfusion inhomogeneity during early tumor growth in rats. Journal of the National Cancer Institute. 1979; 62 (2):387–95. [PubMed: 283271]

Erber R, Eichelsbacher U, Powajbo V, Korn T, Djonov V, Lin J, Hammes HP, Grobholz R, Ullrich A, Vajkoczy P. Ephb4 controls blood vascular during postnatal angiogenesis. The EMBO Journal. 2006; 25:628–641. [PubMed: 16424904]

Ferretti S, Allegrini P, Becquet M, McSheehy P. Tumor interstitial fluid pressure as an early-response marker for anticancer therapeutics. Neoplasia. 2009; 11:874–881. [PubMed: 19724681]

Folkman J. Tumor angiogenesis: therapeutic implications. N Engl J Med. 1971; 285:1182–6. [PubMed: 4938153]

Frieboes H, Chaplain M, Thompson A, Bearer E, Lowengrub J, Cristini V. Physical oncology: a bench-to-bedside quantitative and predictive approach. Cancer Res. 2011; 71:298–302. [PubMed: 21224346]

Frieboes H, Jin F, Chuang Y, Wise S, Lowengrub J, Cristini V. Three-dimensional multispecies tumor growth-ii: tumor invasion and angiogenesis. J Theor Biol. 2010; 264:1254–1278. [PubMed: 20303982]

Friedman A, Lolas G. Analysis of a mathematical model of tumor lymphangiogenesis. Mathematical Models and Methods in Applied Sciences. 2005; 15:95–107.

Fukumura D, Xu L, Takeshi Gohongi YC, Seed B, Jain RK. Hypoxia and acidosis independently up-regulate vascular endothelial growth factor transcription in brain tumors in vivo. Cancer Res. 2001; 61:6020. [PubMed: 11507045]

Fung, YC. Biomechanics: circulation. 2. Springer, University of California; San Diego: 1997.

Gavard J, Gutkind JS. Vegf controls endothelial-cell permeability by promoting the beta-arrestin-dependent endocytosis of ve-cadherin. Nature Cell Biology. 2006; 8:1223–1234.

Greene J, Cheresh D. Vegf as an inhibitor of tumor vessel maturation: implications for cancer therapy. Exp Opinion Biol Therapy. 2009; 9:1347–1356.

Harpold H Jr, EA, Swanson K. The evolution of mathematical modeling of glioma proliferation and invasion. J Neuropathol Exp Nerol. 2007; 66:1–9.

Hashizume H, Baluk P, Morikawa S, McLean J, Thurston G, Roberge S, Jain R, McDonald D. Openings between defective endothelial cells explain tumor vessel leakiness. Am J Pathol. 2000; 156:1363–1380. [PubMed: 10751361]

Hellström M, Phng L, Gerhardt H. Vegf and notch signaling: the yin and yang of angiogenic sprouting. Cell Adh Migr. 2007; 1 (3):133–6. [PubMed: 19262131]

Holash J, Maisonpierre PC, Compton D, Boland P, Alexander CR, Zagzag D, Yancopoulos GD, Wiegand SJ. Vessel cooption, regression, and growth in tumors mediated by angiopoietins and vegf. Science. 1999a; 284:1994–8. [PubMed: 10373119]

Holash J, Wiegand SJ, Yancopoulos GD. New model of tumor angiogenesis: dynamic balance between vessel regression and growth mediated by angiopoietins and vegf. Oncogene. 1999b; 18:5356–62. [PubMed: 10498889]

Intaglietta M, Johnson PC, Winslow RM. Microvascular and tissue oxygen distribution. Cardiovascular Research. 1996; 32 (4):632–643. [PubMed: 8915182]

Jain R. Delivery of molecular medicine to solid tumors: lessons from in vivo imaging of gene expression and function. J Control Release. 2001; 74:7–25. [PubMed: 11489479]

Jain RK. Transport of molecules in the tumor interstitium: a review. Cancer Research. 1987a; 47:3039–3051. [PubMed: 3555767]

Jain RK. Transport of molecules across tumor vasculature. Cancer Metastasis Rev. 1987b; 6:559–593. [PubMed: 3327633]

Jain RK. Delivery of molecular and cellular medicine to solid tumors. Adv Drug Deliv Rev. 2001; 46:149–168. [PubMed: 11259838]

Jain RK. Normalization of tumor vasculature: an emerging concept in antiangiogenic therapy. Science. 2005a; 307:58. [PubMed: 15637262]

Jain RK. Normalization of tumor vasculature: an emerging concept in antiangiogenic therapy. Science. 2005b; 307:58–62. [PubMed: 15637262]

Jain RK, Tong RT, Munn LL. Effect of vascular normalization by antiangiogenic therapy on interstitial hypertension, peritumor edema, and lymphatic metastasis: insights from a mathematical model. Cancer Research. 2007; 67:2729–2735. [PubMed: 17363594]

Jakobsson L, Bentley K, Gerhardt H. Vegfrs and notch: a dynamic collaboration in vascular patterning. Biochemical Society Transactions. 2009; 37:1233–1236. [PubMed: 19909253]

Lee D-S, Bartha K, Rieger H. Flow correlated percolation during vascular remodeling in growing tumors. Physical Review Letter. 2006a; 96:058104.

Lee O, Fueyo J, Xu J, Yung W, Lemoine M, Lang F, Bekele B, Zhou X, Alonso M, Aldape K, Fuller G, Gomez-Manzano C. Sustained angiopoietin-2 expression disrupts vessel formation and inhibits glioma growth. Neoplasia. 2006b; 8:419–428. [PubMed: 16790091]

Levick JR. Flow through interstitium and other fibrous matrices. Quarterly Journal of Experimental Phsyiology. 1987; 72:409–438.

Levick JR, Michel CC. Microvascular fluid exchange and the revised starling principle. Cardiovascular Research. 2010; 87:198–210. [PubMed: 20200043]

Lowengrub J, Frieboes H, Jin F, Chuang YL, Li X, Macklin P, Wise S, Cristini V. Nonlinear modeling of cancer: bridging the gap between cells and tumors. Nonlinearity. 2010; 23:R1–R91. [PubMed: 20808719]

Lunt S, Fyles A, Hill R, Milosevic M. Interstitial fluid pressure in tumors: therapeutic barrier and biomarker of angiogenesis. Future Oncology. 2008; 4:793–802. [PubMed: 19086846]

Macklin P, Lowengrub J. Evolving interfaces via gradients of geometry-dependent interior poisson problems: application to tumor growth. J Comput Phys. 2005; 203 (1):191–220.

Macklin P, Lowengrub J. An improved geometry-aware curvature discretization for level set methods: application to tumor growth. J Comput Phys. 2006; 215 (2):392–401.

Macklin P, Lowengrub J. Nonlinear simulation of the effect of microenvironment on tumor growth. J Theor Biol. 2007; 245 (4):677–704. [PubMed: 17239903]

Macklin P, Lowengrub J. A new ghost cell/level set method for moving boundary problems: application to tumor growth. J Sci Comput. 2008; 35:266–299. [PubMed: 21331304]

Macklin P, McDougall S, Anderson ARA, Chaplain MAJ, Cristini V, Lowengrub J. Multiscale modelling and nonlinear simulation of vascular tumour growth. Journal of Mathematical Biology. 2009; 58:765–798. [PubMed: 18781303]

McDougall SR, Anderson ARA, Chaplain MAJ. Mathematical modelling of dynamic adaptive tumour-induced angiogenesis: clinical implications and therapeutic targeting strategies. Journal of Theoretical Biology. 2006; 241:564–589. [PubMed: 16487543]

McDougall SR, Anderson ARA, Chaplain MAJ, Sherratt JA. Mathematical modelling of flow through vascular networks: implications for tumour-induced angiogenesis and chemotherapy strategies. Bull Math Biol. 2002; 64:673–702. [PubMed: 12216417]

Milosevic M, Lunt S, Leung E, Skliarenko J, Shaw P, Fyles A, Hill R. Interstitial permeability and elasticity in human cervix cancer. Microvasc Res. 2008; 75:381–390. [PubMed: 18187164]

Minchinton AI, Tannock I. Drug penetration in solid tumours. Nature Rev Cancer. 2006; 6:583. [PubMed: 16862189]

Padera TP, Stoll BR, Tooredman JB, Capen D, di Tomaso E, Jain RK. Cancer cells compress intratumor vessels. Nature. 2004; 427:695. [PubMed: 14973470]

Pepper, MS.; Lolas, G. The lymphatic vascular system in lymphangiogenesis invasion and metastasis a mathematical approach. In: Bellomo, N., editor. Selected Topics in Cancer Modeling. Modeling and Simulation in Science, Engineering and Technology. Birkhaeuser; 2008. p. 1-22.

Phipps C, Kohandel M. Mathematical model of the effect of interstitial fluid pressure on angiogenic behavior in solid tumors. Computational and Mathematical Methods in Medicine. 2011; 2011

Pries A, Cornelissen A, Sloot A, Hinkeldey M, Dreher M, Hoepfner M, Dewhirst M, Secomb T. Structural adaptation and heterogeneity of normal and tumor microvascular networks. PLoS Comp Biol. 2009; 5:e1000394.

Pries AR, Hopfner M, le Noble F, Dewhirst MW, Secomb TW. The shunt problem: control of functional shunting in normal and tumour vasculature. Nature Reviews Cancer. 2010; 10:587–593.

Pries AR, Neuhaus D, Gaehtgens P. Blood viscosity in tube flow: dependence on diameter and hematocrit. Am J Physiol Heart Circ Physiol. 1992; 263:H1770–H1778.

Pries AR, Secomb TW, Gaehtgens P. Structural adaptation and stability of microvascular networks: theory and simulations. Am J Physiol Heart Circ Physiol. 1998; 275:H349–H360.

Raza A, Franklin M, Dudek A. Pericytes and vessel maturation during tumor angiogenesis and metastasis. Am J Hematology. 2010; 85:593–598.

Roose T, Chapman SJ, Maini P. Mathematical models of avascular tumor growth. SIAM Review. 2007; 49:179–208.

Shieh AC, Swartz MA. Regulation of tumor invasion by interstitial fluid flow. Phys Biol. 2011; 8:051021.

Shields JD, Fleury ME, Yong C, Tomei AA, Randolph GJ, Swartz MA. Autologous chemotaxis as a mechanism of tumor cell homing to lymphatics via interstitial flow and autocrine ccr7 signaling. Caner Cell. 2007; 11:526–538.

Stephanou A, Mcdougall S, Anderson A, Chaplain M. Mathematical modelling of flow in 2d and 3d vascular networks: applications to anti-angiogenic and chemotherapeutic drug strategies. Mathematical and Computer Modelling. 2005; 40 (10):1137–1156.

Stoll BR, Migliorini C, Kadambi A, Munn LL, Jain RK. A mathematical model of the contribution of endothelial progenitor cells to angiogenesis in tumors: implications for antiangiogenic therapy. Blood. 2003; 102 (7):2555–2561. [PubMed: 12775571]

Tong RT, Boucher Y, Kozin SV, Winkler F, Hicklin DJ, Jain RK. Vascular normalization by vascular endothelial growth factor receptor 2 blockade induces a pressure gradient across the vasculature and improves drug penetration in tumors. Cancer Research. 2004; 64:3751–6.

Tredan O, Galmarini C, Patel K, Tannock I. Drug resistance and the solid tumor microenvironment. J Nat Cancer Inst. 2007; 99:1441–1454. [PubMed: 17895480]

Ventura A, Jacks T. Micrornas and cancer: short rnas go a long way. Cell. 2009; 136 (4):586–591. [PubMed: 19239879]

Welter M, Bartha K, Rieger H. Emergent vascular network inhomogeneities and resulting blood flow patterns in a growing tumor. Journal of Theoretical Biology. 2008; 250:257–280. [PubMed: 17996256]

Welter M, Bartha K, Rieger H. Vascular remodelling of an arterio-venous blood vessel network during solid tumour growth. Journal of Theoretical Biology. 2009; 259:405–422. [PubMed: 19371750]

Welter M, Bartha K, Rieger H. Physical determinants of vascular network remodeling during tumor growth. Eur Phys J E. 2010; 33:149–163. [PubMed: 20607341]

Williams CK, Li JL, Murga M, Harris AL, Tosato G. Up-regulation of the notch ligand delta-like 4 inhibits vegf-induced endothelial cell function. Blood. 2006; 107:931–939. [PubMed: 16219802]

Zheng X, Wise S, Cristini V. Nonlinear simulation of tumor necrosis, neo-vascularization and tissue invasion via an adaptive finite-element/level-set method. Bulletin of Mathematical Biology. 2005; 67:211–259. [PubMed: 15710180]

A Microenvironment interactions

In vascular tumor growth, the viable tumor cells and endothelial cells (ECs) remodel the extracellular matrix (ECM) by releasing degrading proteolytic enzymes. Following previous work (Macklin *et al.*, 2009), we model the tumor microenvironment by introducing E representing the extracellular matrix density (ECM) and M representing the level of degrading proteolytic enzymes (MDE) which are assumed to satisfy (Macklin *et al.*, 2009):

$$\frac{\partial M}{\partial t} = \nabla \cdot (D_M \nabla M) + \overline{\lambda}_{prod}^M (1-M)\mathbf{1}_{\Omega_V} - \overline{\lambda}_{decay}^M M + \overline{\lambda}_{spr.prod}^M \mathbf{1}_{sprouttips} \quad (32)$$

$$\frac{\partial E}{\partial t} = -\overline{\lambda}_{degradation}^E EM + \overline{\lambda}_{prod}^E (1-E)\mathbf{1}_{\Omega_V} + \overline{\lambda}_{spr.prod}^E \mathbf{1}_{sprouttips} \quad (33)$$

The MDEs are produced by the viable tumor cells ($\Omega_V = \Omega_P \cup \Omega_H$) and neo-vascular sprouts with the rates $\overline{\lambda}_{prod}^M$ and $\overline{\lambda}_{spr>prod}^M$, respectively. For simplicity, we assume only the sprouting ECs release MDEs which diffuse into the microenvironment with constant but small D_M and decay with the rate $\overline{\lambda}_{decay}^M$. We assume that MDE used up in the interaction with the ECM with the rate $\overline{\lambda}_{degradation}^E$ are negligible with the MDE production, thus the term $-\overline{\lambda}_{degradation}^E EM$ only applies to the dynamics of ECM, which can also be produced by the

viable tumor cells and tip ECs with the rates $\overline{\lambda}_{prod}^{M}$ and $\overline{\lambda}_{spr.prod}^{M}$, respectively. We also take the zero Neumann boundary condition $\dfrac{\partial M}{\partial n}=0$ in the computation of MDE.

B Tumor angiogenesis factors

When tumor cells become hypoxic, they release tumor angiogenesis factors (TAF, e.g., members of the VEGF family). Here, we assume TAFs are released by hypoxic tumor cells with rate $\bar{\lambda}_{prod}$, diffuse into the tissue with constant diffusion coefficient D_T, are uptaken by surrounding ECs with rate $\overline{\lambda}_{binding}^{T}$, and decay of a constant rate $\overline{\lambda}_{decay}^{T}$. Thus, we have the following (Macklin *et al.*, 2009):

$$0=\nabla \cdot (D_T \nabla T)+\overline{\lambda}_{prod}^{T}(1-T)\mathbf{1}_{\Omega_H} -\overline{\lambda}_{decay}^{T}T-\overline{\lambda}_{binding}^{T}\mathbf{1}_{vessel} \quad (34)$$

In the far-field at the boundary of the computational domain, we take Neumann boundary conditions: $\dfrac{\partial T}{\partial n}=0$

C The effect of ECM on χE and μE

The tumor response to pressure and *ECM* adhesion gradients are mediated by hetereogeneous sensitivities, which are modeled using non-constant cell-mobility and haptotaxis coefficients. We follow (Macklin *et al.*, 2009), who postulate a certain level of *ECM* required for focal adhesion-based migration (too much focal contact strength could retard the detachment of cell's trailing edge from the *ECM*), and specify the haptotaxis coefficient as a non-monotone function of E:

$$\chi_E = \begin{cases} \overline{\chi}_{E,min} & E < \overline{E}^{\chi}_{mincuttoff} \\ p_{\chi}(E) & \overline{E}^{\chi}_{mincutoff} \le E \le \overline{E}^{\chi}_{maxcutoff} \\ \overline{\chi}_{E,min} & E \ge \overline{E}^{\chi}_{maxcutoff} \end{cases}$$

where p_{χ} is a non-monotone interpolating function. See details for other parameters in Table (3).

As in (Macklin *et al.*, 2009), we take μ_E to be a monotone decreasing function of *E*:

$$\mu_E = \begin{cases} \overline{\mu}_{max} & E < \overline{E}^{\mu}_{mincuttoff} \\ p_{\mu}(E) & \overline{E}^{\mu}_{mincutoff} \le E \le \overline{E}^{\mu}_{maxcutoff} \\ \overline{\mu}_{min} & E \ge \overline{E}^{\mu}_{maxcutoff} \end{cases}$$

where p_{μ} is a smooth interpolating function. See details for other parameters in Table (3).

Highlights

- We study interstitial fluid pressure/flow (IFP/IFF) during vascular tumor growth.

- Vessel collapse results in transport barriers and decreased tumor growth rate.

- High interstitial hydraulic conductivity leads to plateau profile in tumor IFP.

- Increasing vascular hydraulic conductivity maintains high IFP in tumor.

- Tumor vascular pathologies promote local invasion and metastasis through IFF.
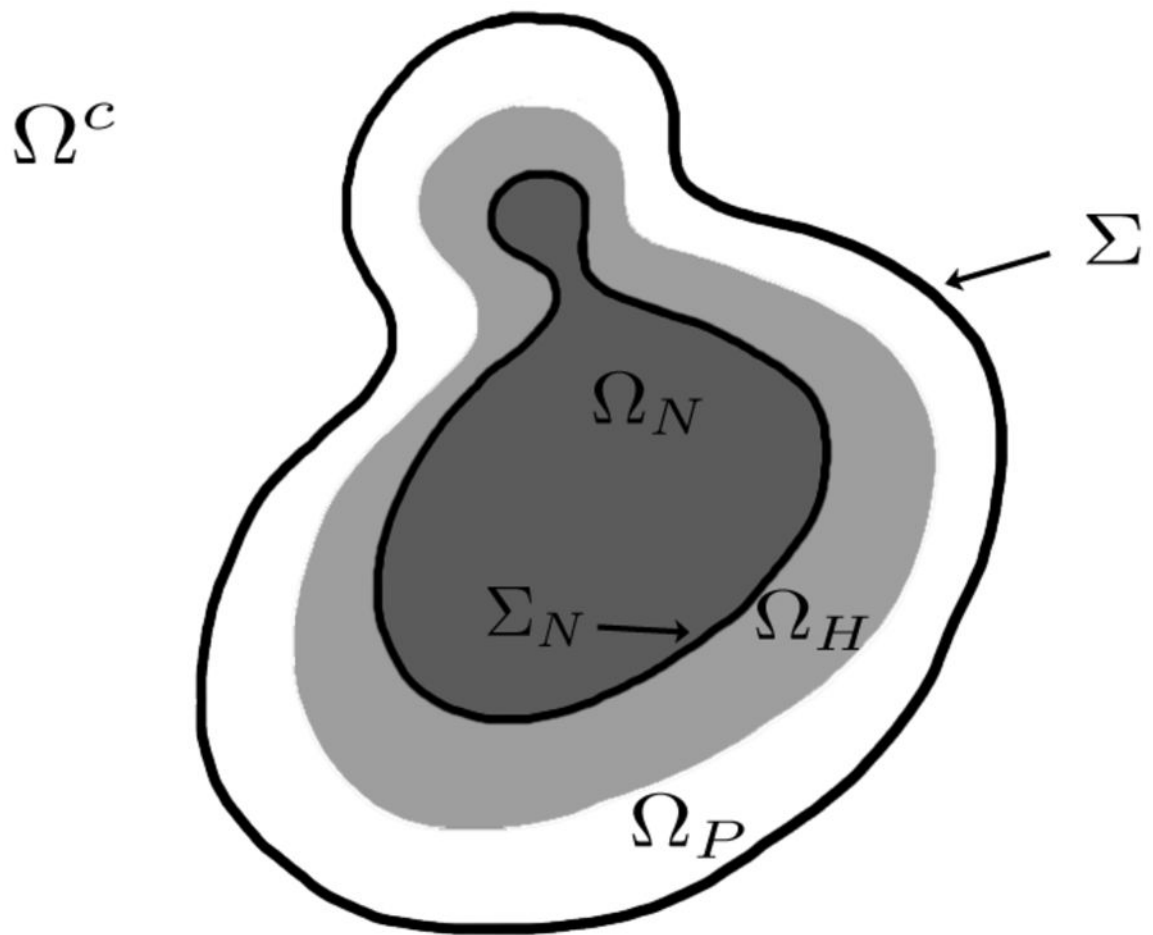
Figure 1.
Schematic description of the tumor.
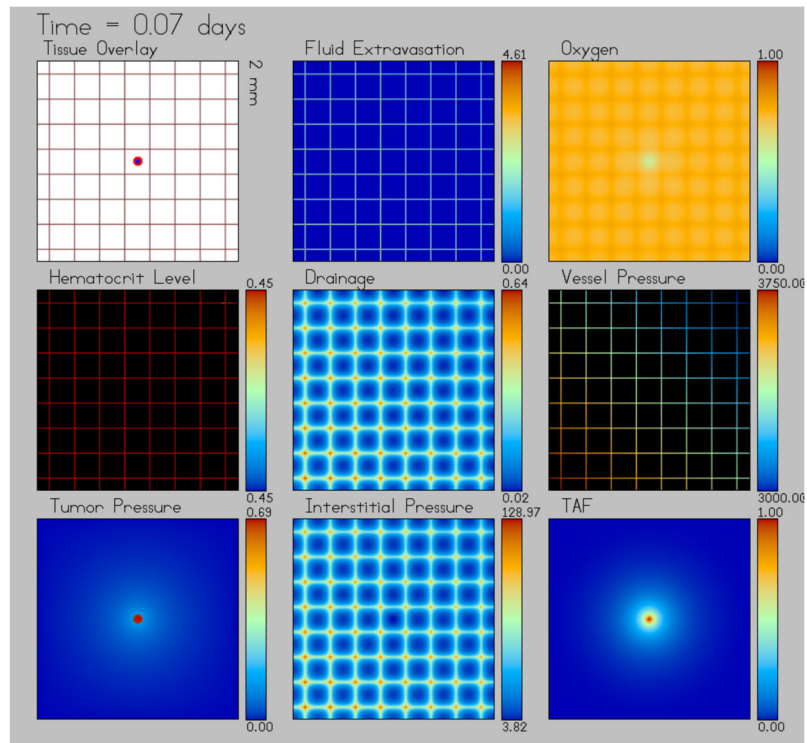
Figure 2.
Tumor growth at day 0.07: a small avascular tumor (Row 1, Column 1) is placed at the center of the domain. As the tumor grows, the oxygen concentration in the interior decreases and cells become hypoxic (blue) and necrotic (brown in Figs.4-6). Hypoxic cells (blue in Row 1, Column 1) release TAF into the domain (Row 3, Column 3). Vessel pressure (Row 2, Column 3) on the boundary starts with 3750 Pa.s at the lower left and 3000 Pa.s at the upper right with linear increments in between. The 16 vessel nodes along the left and bottom boundaries are inlets while the other 16 vessel nodes along the right and top boundaries are outlets. Red blood cells (RBCs) are transported along the blood stream carrying oxygen, which is quantified by the hematocrit level (Row 2, Column 1). Oxygen (Row 1, Column 3) is calibrated ($\sigma = 0.76 \sim 1$) to support normal tissue metabolism. Since the tumor uptakes more oxygen than the surrounding tissue, the oxygen level in the tumor region is smaller. The vessels extravasate fluid (Row 1, Column 2) and the fluid is drained (Row 2, Column 2) by functional lymphatic vessels. Slightly higher interstitial pressure (Row 3, Column 2) can be seen to coincide with the vasculature.
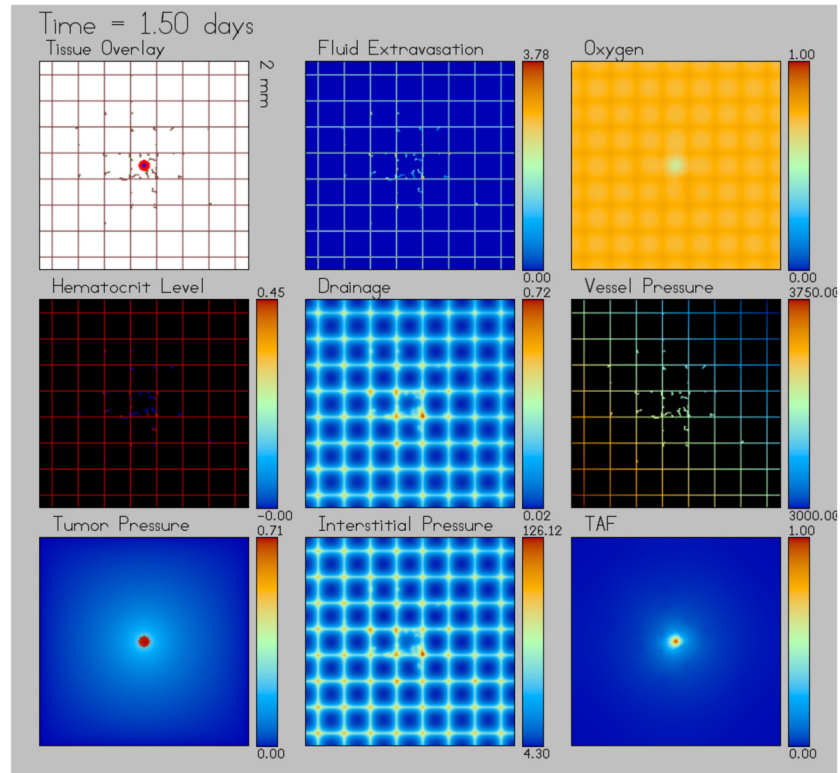
Figure 3.
Tumor growth at day 1.50: vessel sprouts form (Row 1, Column 1), which have not yet anastomosed near the tumor in order to provide large enough flow to transport RBCs (Row 2, Column 1). Note the discrepancy between the newly updated vasculature and the full hematocrit level (0.45) coverage. However, fluid is extravasated (Row 1, Column 2) from newly formed vessels even before anastomosis begins.
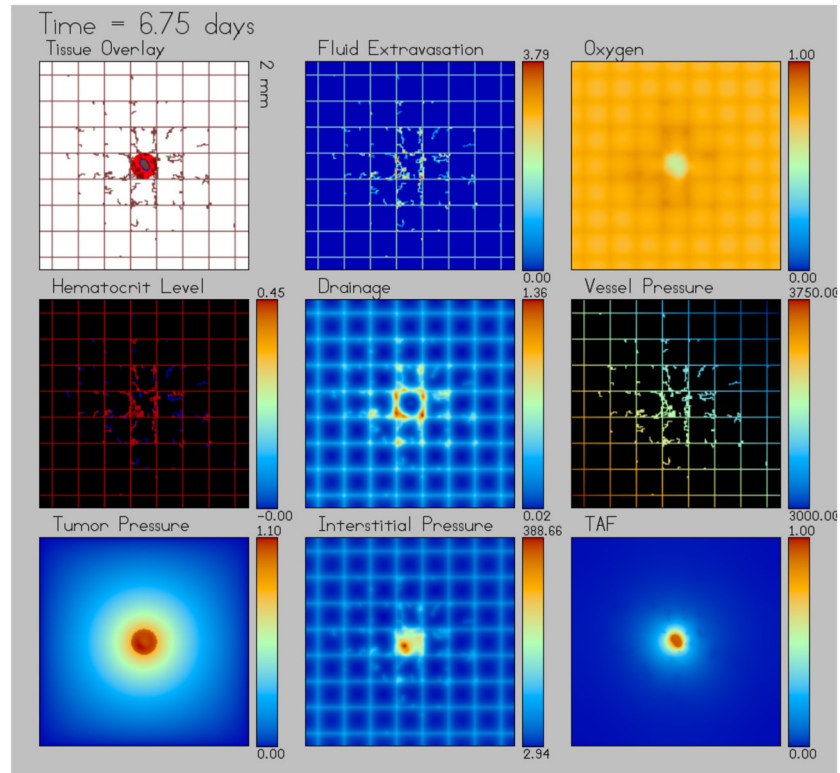
Figure 4.
Tumor growth at day 6.75: growth and angiogenesis continue and new loops in the neovasculature (Row 1, Column 1) are formed enabling vascular flow (Row 2, Column 1), thus leading to a higher oxygen concentration (Row 1, Column 3) near the tumor. As a result, the hydrostatic pressure (Row 3, Column 1) in the interior further increases and reaches around 1.10, which is larger than $KL_{min} = 0.75$ in the lymphatic drainage function $c(P_c,L)$. The IFP in the tumor is then elevated because of more fluid extravasation from the neovasculature as well as the decrease in drainage (Row 2, Column 2) by the degrading lymphatic density L and lowering of hydrostatic pressure P_c.
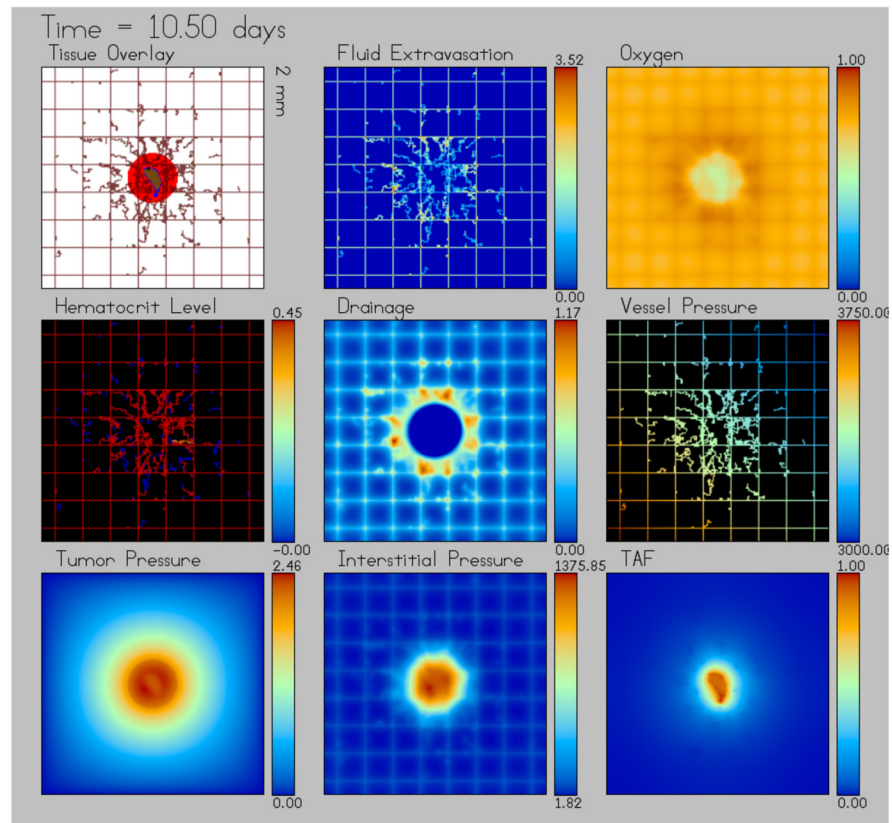
Figure 5.
Tumor growth at day 10.5: there is little lymphatic drainage (Row 2, Column 2) in the tumor interior. Oxygen (Row 1, Column 3) is elevated outside the tumor. The IFP increases (Row 3, Column 2) significantly, reflecting the inhibited drainage of the interstitial fluid by both degradation of the lymphatics and pressure-induced lymphatic collapse.
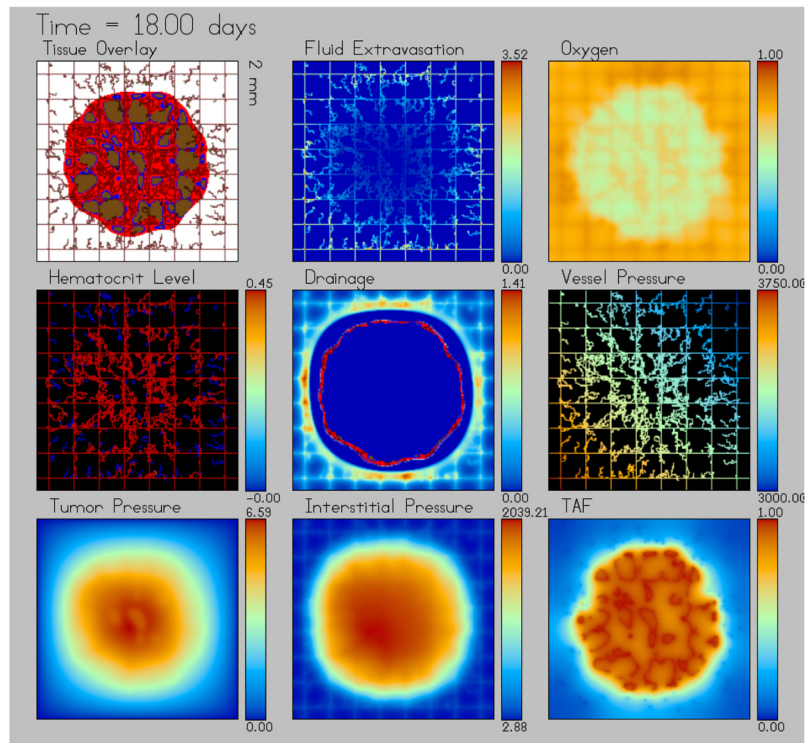
Figure 6.
Tumor growth at day 18.0: the tumor is approximately 1.5 mm in diameter. The drainage occurs at a small distance from the tumor-host boundary (see the boundary projected on the drainage plot in Row 2, Column 2). Oxygen (Row 1, Column 3), vessel pressure (Row 2, Column 3) and TAF (Row 3, Column 3) distributions become progressively more heterogeneous as a result of the interplay between the growing tumor and the vasculature. The heterogeneous oxygen distribution leads to inhomogeneous distributions of hypoxic and necrotic cells (Row 1, Column 1), which in turn leads to inhomogeneous distribution of TAF and vessel sprouts. The elevated IFP (Row 3, Column 2) reaches into the surrounding tissue where there is little drainage.
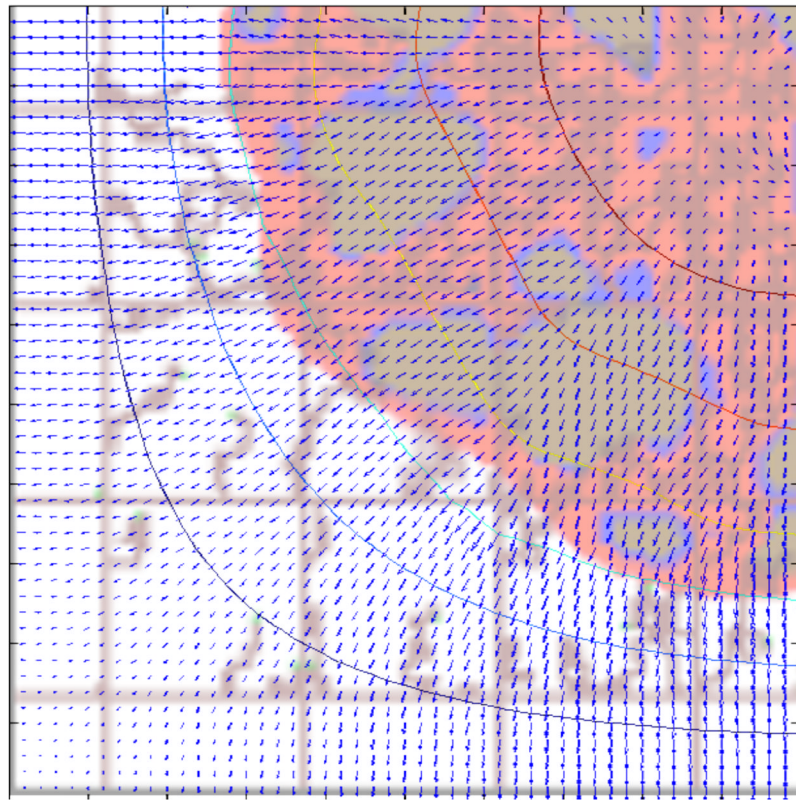
Figure 7.
Cell velocity with hydrostatic pressure contours from Fig. 6: the pressure drops approximately linearly from the inside of the tumor to the outside, and the velocity is generally outward except at the tumor interior where this velocity is directed towards the necrotic region (see arrows at the upper right corner).
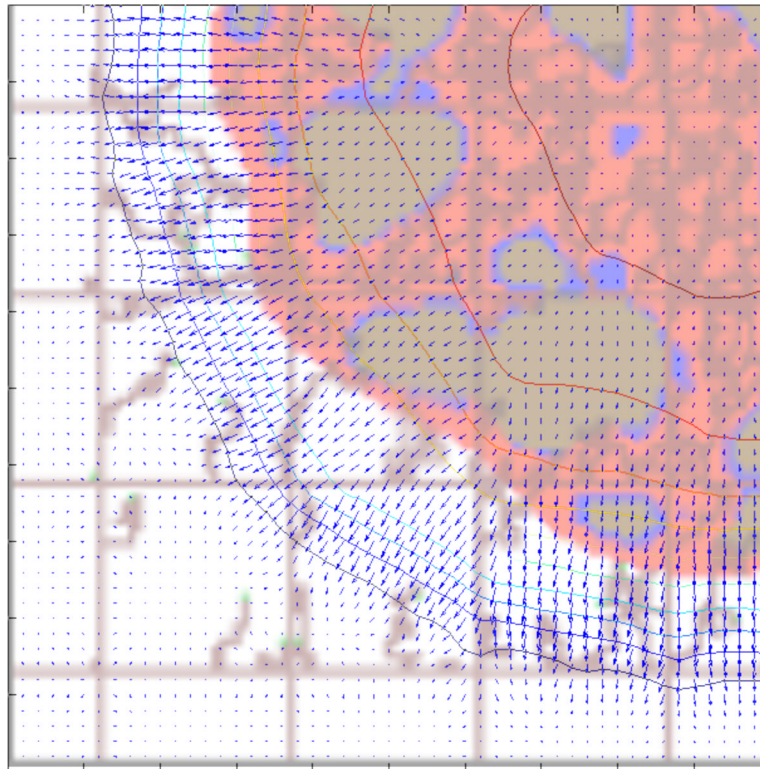
Figure 8.
Interstitial fluid velocity with IFP contours from Fig. 6: In the well drained tissue, the interstitial fluid velocity direction is pointing from the vasculature locations to the avascular regions. At the interface region where the IFP level changes steeply, the fluid velocity is towards the well-drained regions and the speed is the largest. Inside the drainage-free area, the fluid velocity is extremely small.
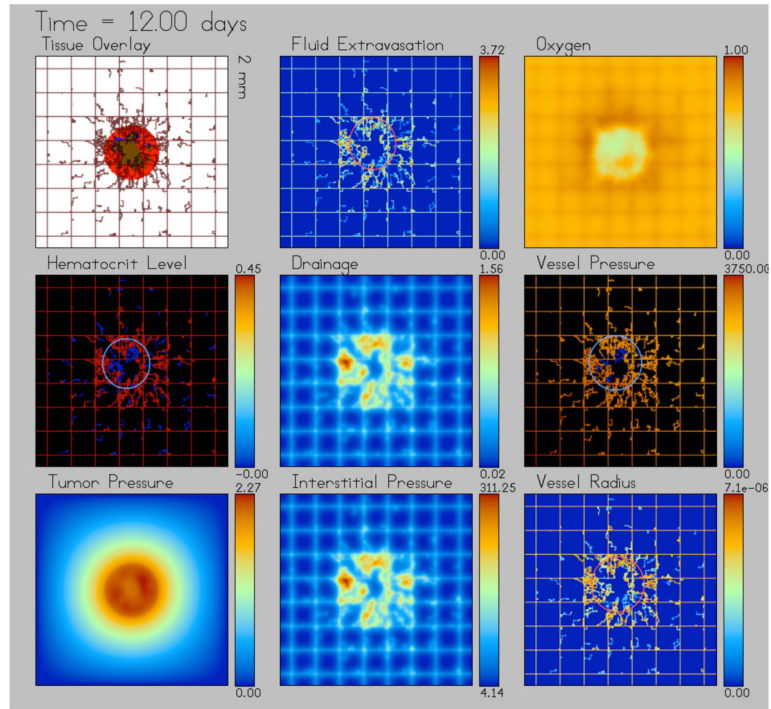
Figure 9.
Tumor growth at day 12.0 for $P_{CT} = 2.0$ with fully functional lymphatic vessels: vessel collapse is mainly confined to the tumor interior, resulting in zero vessel radius (highlighted by the red oval), zero blood vessel pressure (highlighted by the light blue oval), zero hematocrit level (highlighted by the light blue oval) and zero fluid extravasation (highlighted by the red circle).
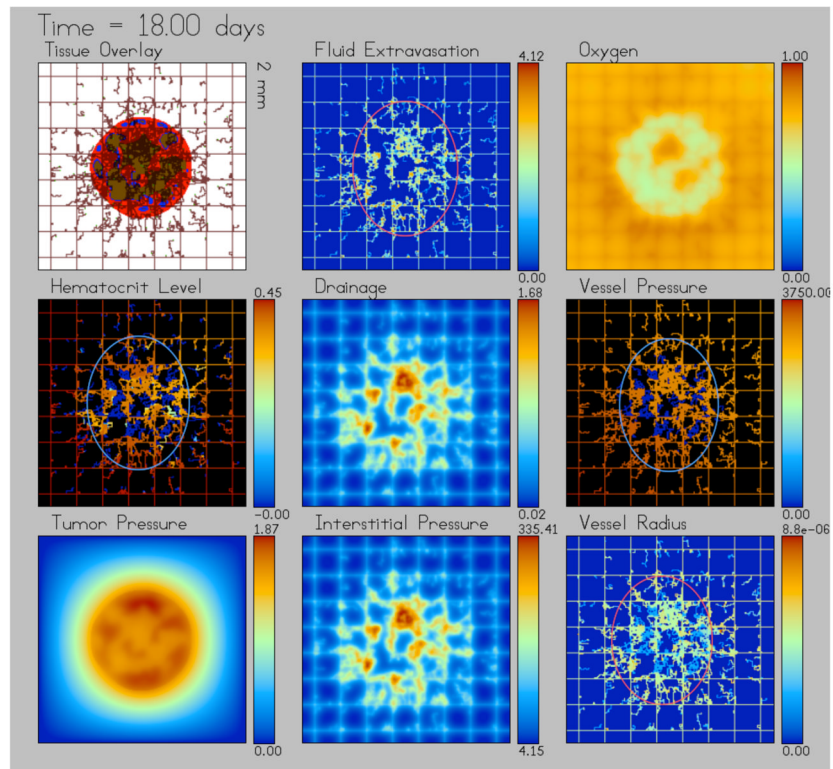
Figure 10.
Tumor growth at day 18.0 for $P_{CT} = 2.0$ with fully functional lymphatic vessels: as the tumor grows, vessels in the tumor microenvironment collapse (the ovals depict where vessels have collapsed), resulting in zero blood vessel pressure (highlighted by the light blue oval), zero hematocrit level (highlighted by the light blue oval) and zero fluid extravasation (highlighted by the red oval). The hematocrit level near the collapsed region is decreased due to the decrease in flow after vessel collapse.
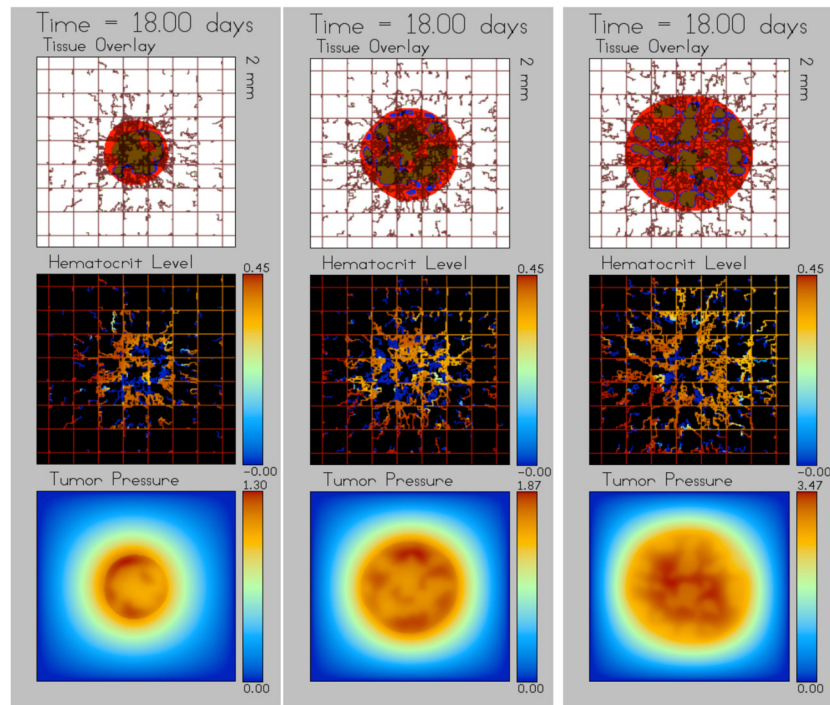
Figure 11.
Tumor growth at day 18 varying P_{CT}. (Column 1: $P_{CT} = 1$, Column 2: $P_{CT} = 2$ and Column 3: $P_{CT} = 3$.) Tumor size and pressure increase as P_{CT} increases, while the zero hematocrit level region expands as P_{CT} decreases.
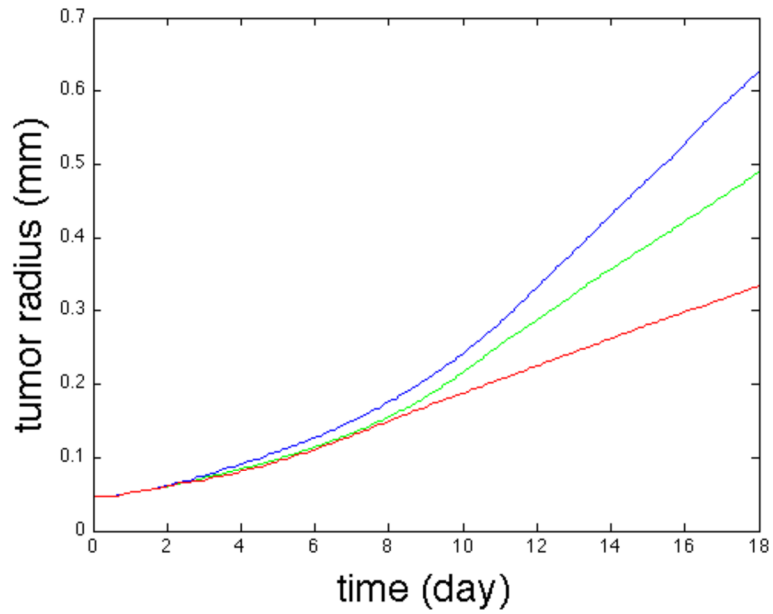
Figure 12.
The effective tumor radius vs. time for different blood vascular resistances P_{CT} and fully functional lymphatics $c(P,L) = 1$. Here, $P_{CT} = 1$ (blue), $P_{CT} = 2$ (green) and $P_{CT} = 3$ (red) are shown. The growth speed increases with P_{CT}. The effective radius is computed by

$$\sqrt{\frac{Tumor\,Area}{\pi}}.$$
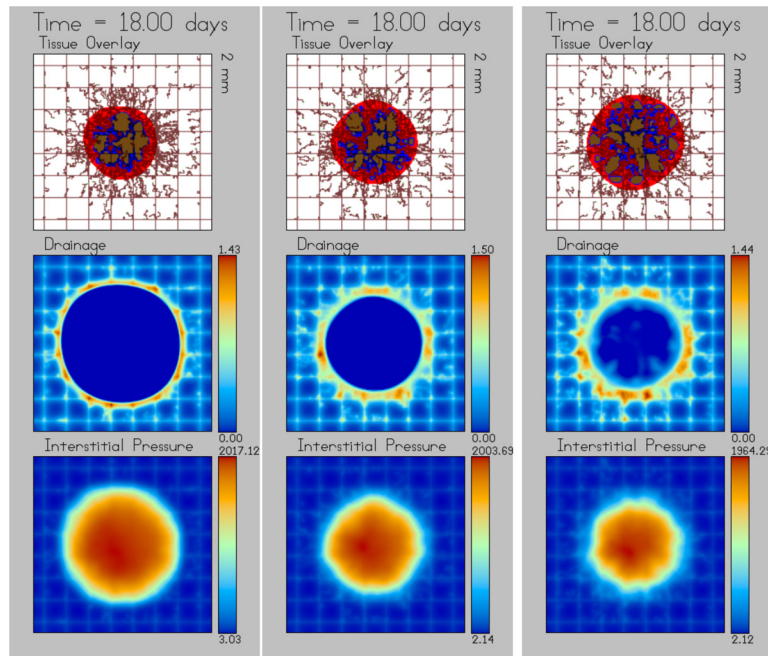
Figure 13.
Tumor growth at day 18 with varying KL_{max}. (Column 1: $KL_{max} = 1$, Column 2: $KL_{max} = 2$ and Column 3: $KL_{max} = 3$). Tumor size increases with KL_{max}, while the drainage-free zone expands and the tumor IFP decreases as KL_{max} increases.
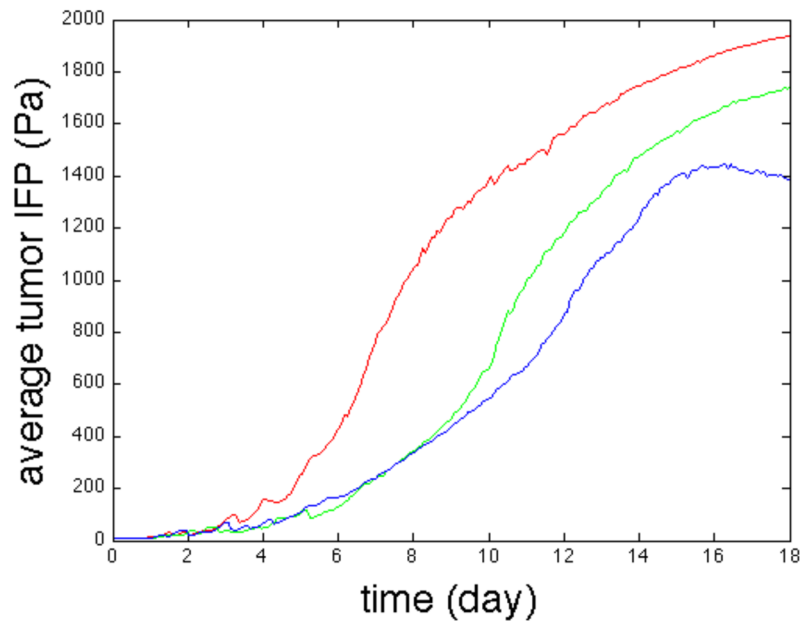
Figure 14.
Tumor IFP average for different lymphatic resistances KL_{max} for fully functional blood vasculatures (e.g., $P_{CT} = \infty$). Here, $KL_{max} = 1$ (red), $KL_{max} = 2$ (green) and $KL_{max} = 3$ (blue) are shown. The average IFP decreases as KL_{max} increases.
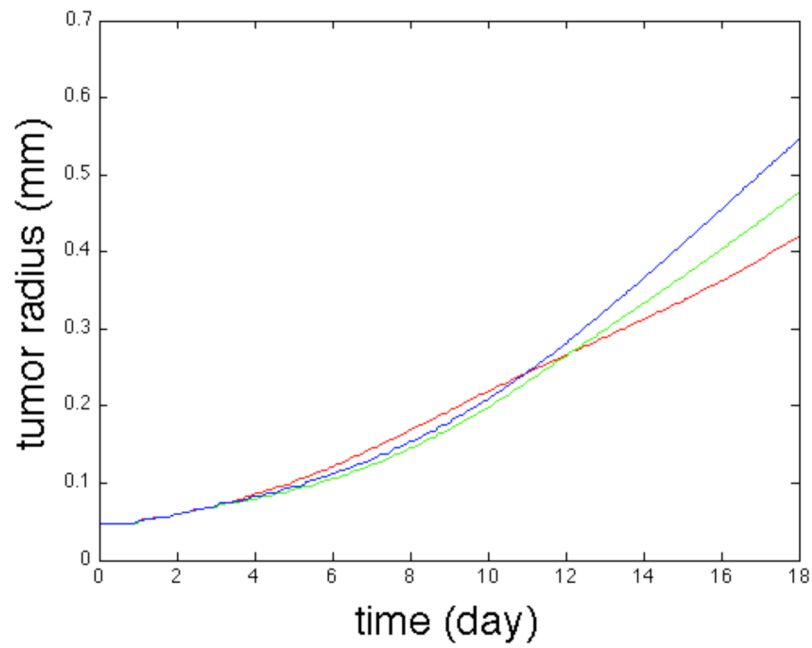
Figure 15.
The effective tumor radiii for different KL_{max} from Fig. 14 ($KL_{max} = 1$ in red, $KL_{max} = 2$ in green and $KL_{max} = 3$ in blue). At late times (e.g., $t \approx 18$), the growth rate increases as KL_{max} increases, due to the inhibitory effect of IFP on oxygen extravasation. The behavior at early times (e.g., $t \lesssim 10$) is influenced by stochastic effects.
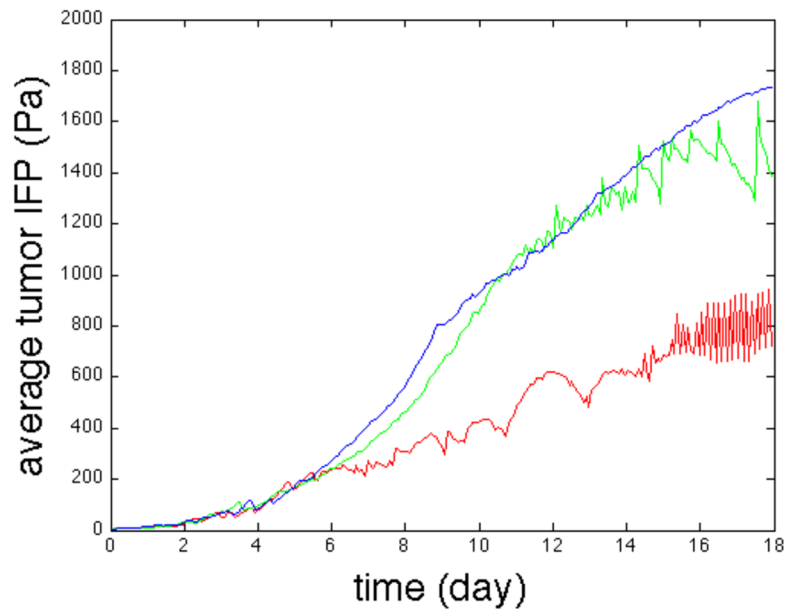
Figure 16.
The average IFP in the tumor vs. time with $KL_{max} = 2$ and different blood vessel collapse resistances P_{CT} ($P_{CT} = 1$ in blue, $P_{CT} = 2$ in green and $P_{CT} = 3$ in red). The IFP average still increases as P_{CT} increases, but saturates as P_{CT} exceeds KL_{max}. The oscillation in the curves $P_{CT} = 1$ and $P_{CT} = 2$ results from the vessel recovery and collapse, and is an artifact of the simulation caused by not solving for the vessel radii implicitly. For the case $P_{CT} = 3$, no blood vessels collapse since the tumor pressure P_c never exceeds 3 because the IFP impedes nutrient extravasation and tumor cell proliferation.
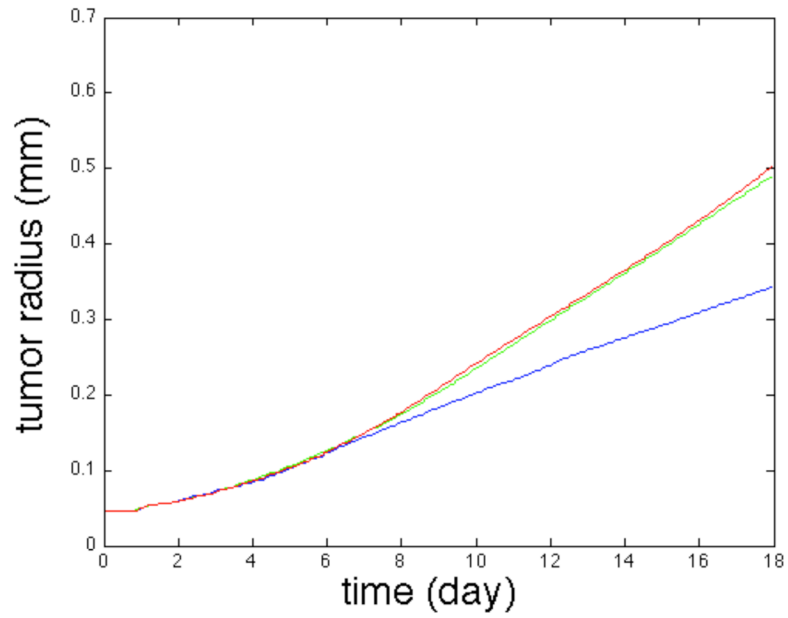
Figure 17.
The effective tumor radius vs. time with $KL_{max} = 2$ and different P_{CT} from Fig. 16 ($P_{CT} = 1$ in blue, $P_{CT} = 2$ in green and $P_{CT} = 3$ in red). The growth rate still increases as P_{CT} increases, but the effect of increasing P_{CT} saturates; compare to Fig. 12 where the lymphatics are fully functional.
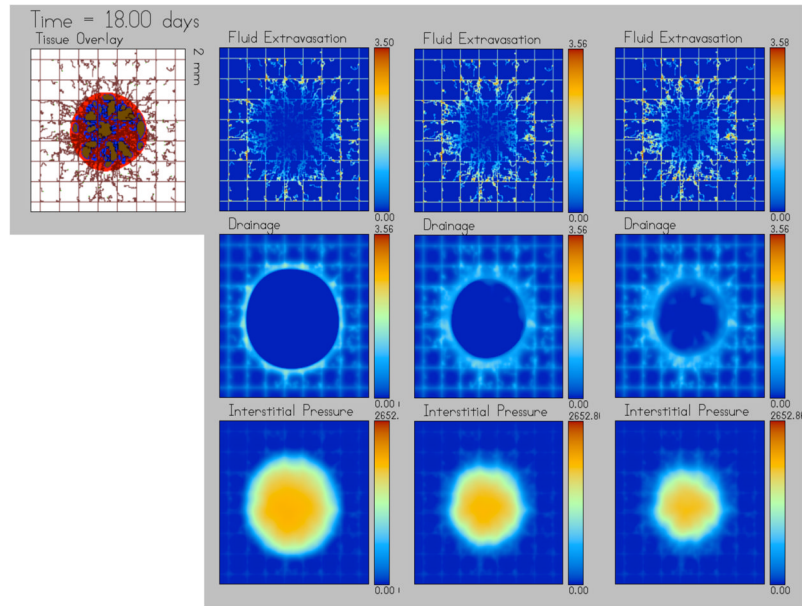
Figure 18.
Control tumor sample at day 18 with different KL_{max} (Column 1: $KL_{max} = 1$, Column 2: $KL_{max} = 2$, Column 3: $KL_{max} = 3$). The tumor and host tissue share the same vascular/ interstitial hydraulic conductivity and osmotic pressure difference. See the red curves in Figs. 19 and 20 for the corresponding cross sectional IFP profile and outward gradient in the tumor center, respectively.
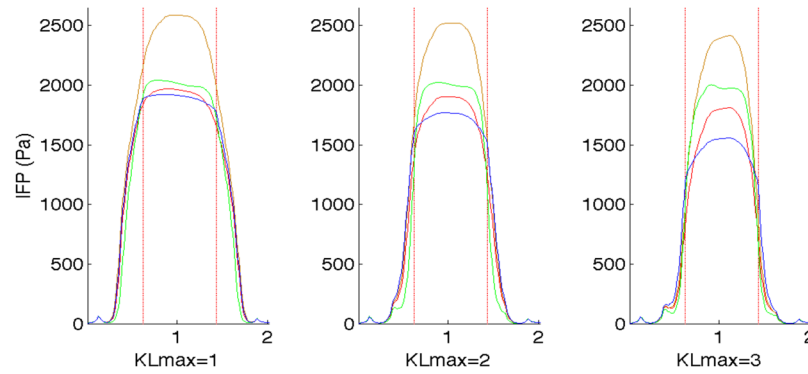
Figure 19.
Cross sectional IFP distribution at y = 1mm (the domain center) with the same tumor and vasculature configurations and different KL_{max} under the following conditions: matched vascular/interstitial hydraulic conductivity and osmotic pressure difference (red curves), attenuated osmotic pressure difference inside the tumor (brown curves), elevated vascular hydraulic conductivity (green curves) and elevated interstitial hydraulic conductivity (blue curves). red The two vertical red lines correspond to the tumor boundary. Compared with the control (red curves), an attenuated osmotic pressure difference (brown) elevates the tumor IFP and is sensitive to changes in lymphatic function; an elevated interstitial hydraulic conductivity (blue) effectively flattens the tumor IFP and presents a plateau profile together when lymphatic function is impaired (KL_{max} = 1); elevated vascular hydraulic conductivity (green) both elevates the IFP and maintains its profile under changes in lymphatic function.
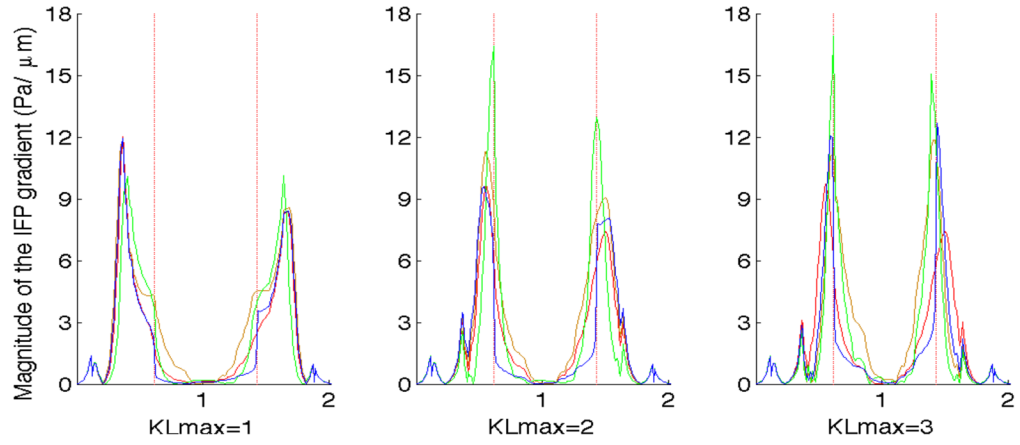
Figure 20.
Cross sectional outward IFP gradient $|\nabla P_i \cdot \mathbf{n}_{out}|$ along y = 1mm (the domain center) under the same conditions as in Fig. 19. red The two vertical red lines correspond to the tumor boundary. In all cases, there is an velocity outward from the tumor, which is small inside the tumor and larger at the tumor boundary, consistent with Fig. 8. The elevated vascular hydraulic conductivity (green curve) contributes to a larger outward gradient at the tumor boundary and an elevated interstitial hydraulic conductivity (blue curve) decreases the outward gradient inside the tumor. The color scheme is the same as in Fig. 19.
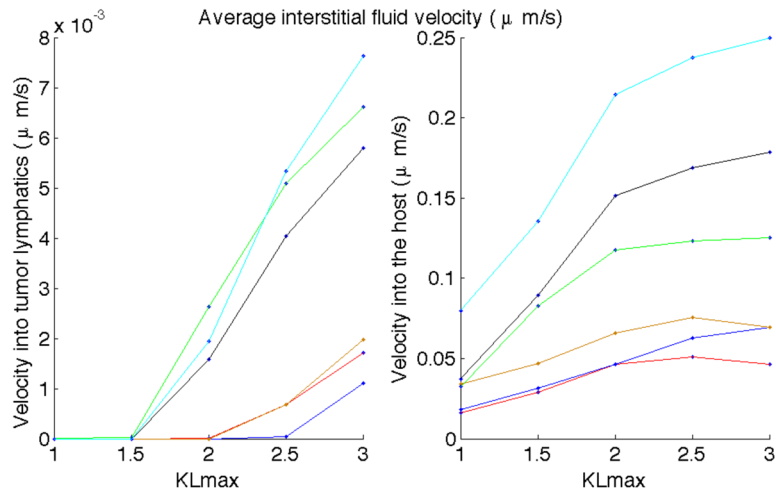
Figure 21.
Quantitative study of average IFF red velocity leaving the tumor through the tumor lymphatics (left) and into the host tissue (right). Cyan: All pathologies considered (attenuated osmotic pressure difference across the vessel wall, elevated vascular and interstitial hydraulic conductivities); Black: Elevated vascular and hydraulic conductivities; Green: Elevated vascular hydraulic conductivity; Brown: Attenuated osmotic pressure difference; Blue: Elevated interstitial hydraulic conductivity; Red: Control. These graphs indicate that the interstitial flow red velocities are most affected by elevated vascular hydraulic conductivity. Note that when $KLmax = 1$, all the lymphatic vessels in the tumor are collapsed so that the rate of IFF removal to the lymphatics is zero. Thus in all cases the IFF is solely directed into the host tissue when $KLmax = 1$. When the interstitial hydraulic conductivity is elevated (blue), redmore interstitial fluid leaves the tumor through the tissue red than through the lymphatics for all $KLmax$ redcompared with control (red) since redmore lymphatic vessels in the tumor are collapsed in this case. Further, the redincrease of IFF redvelocity into the host tissue redsaturates as $KLmax$ increases. See text for further explanation.

Table 1

The parameter values for the lymphatics and *IFP*.

Physiological Name	Parameter	Unit	Values and References
cell volume fraction	φ_c	1	0.5
water volume fraction	φ_f	1	0.5
pressure induced drainage maximum	$Lymmax$	1	1.8
natural draining rate by lymphatics	λ_{fL}	per pa·s	5.0e-6
rate by cell mitosis	λ_M	per s	0.77e-5
characteristic volume	V_T	μm^3	1000
lymph partial collapsing threshold	KL_{min}	1	0.75
lymph collapsing threshold	KL_{max}	1	**1** (left column in Fig. 13, 18–20, red in Fig. 14–15) **2** (Fig. 2–12,16–17 middle column in Fig. 13, Fig. 18–20), green in Fig. 14–15 **3** (right column in Fig. 13, 18–20, blue in Fig. 14–15))
interstitial hydraulic conductivity	K_i	μm^2 per pa·s	0.64e-2 (All except blue curves in Figs. 19 – 21), (Baxter & Jain, 1989) 3.1e-2 (blue curves in Figs. 19 – 21), (Baxter & Jain, 1989)
vessel wall hydraulic conductivity	K_{Vf}	μm per pa·s	0.27e-5, (All except green curves in Figs. 19 – 21), (Baxter & Jain, 1989) 2.1e-5, (green curves in Figs. 19 – 21), (Baxter & Jain, 1989)
osmotic pressure difference	$\omega(\pi_v - \pi_i)$	pa	1333, (All except brown curves in Figs.19 – 21), (Baxter & Jain, 1989) 667, (brown curves in Figs.19 – 21), computed from (Baxter & Jain, 1989)
rate of degradation of lymphatics by *MDE*	λ_{ML}	$1/M^\star$	1.0
σ extravasation sensitivity to P_f	k_{Pf}	1	0 (Fig. 2–8) 0.5 (Fig. 9–21)

Table 2

The key parameter values for the vasculature.

Physiological Name	Parameter	Scaled by or Unit	Values		
response rate of radius to intravascular pressure	k_p	k_{wss}, the response rate of radius to wall shear stress	1.0		
response rate of radius to metabolic stimulus	k_m	k_{wss}	1.0		
natural shrinking tendency of vessel radius	k_s	k_{wss}	2.24		
response rate of radius to tumor pressure	k_{pc}	k_{wss}	0.76		
blood vessel collapsing threshold	P_{CT}	1	**1**	(left column in Fig. 11, red in Fig. 12,16–17)	
			2	(middle column in Fig. 11, green in Fig. 12,16–17)	
			3	(right column in Fig. 11, blue in Fig. 12,16–17)	

Table 3

The tumor model parameter values used in all the simulations (from (Macklin *et al.*, 2009)).

Physiological Name	Parameter	Scaled by or Unit	Values
oxygen diffusion characteristic value of discharge haematocrit	D_σ $\bar{H}_D$	$D_\sigma^\star$, a characteristic dimensional unit as a fraction	1.0 0.45
minimal value needed for oxygen extravasation	$\bar{h}_{min}$	unit as a fraction	0.0
coefficient		oxygen diffusion coefficient	
rate of cell mitosis	λ_M	unit: per s	0.77e-5
characteristic volume	V_T	unit: μm^3	1000
uptake rate of oxygen in proliferating tumor region	λ_{prolif}^σ	$\lambda_\sigma^\star$, the characteristic rate of oxygen uptake in the proliferating tumor region	1.5
uptake rate of oxygen in host microenvironment	λ_{host}^σ	$\lambda_\sigma^\star$	0.12
uptake rate of oxygen in hypoxic tumor region	λ_{hyp}^σ	$\lambda_\sigma^\star$	1.3
decay rate of oxygen in necrotic tumor region	λ_{nec}^σ	$\lambda_\sigma^\star$	0.35
baseline rate of oxygen transfer from vessels	$\bar{\lambda}_{vasc}^\sigma$	$\lambda_\sigma^\star$	0.25
TAF diffusion coefficient	D_T	$D_\sigma^\star$	0.005
production rate of by *TAF* hypoxic tumor cells	$\bar{\lambda}_{prod.}^T$	$\lambda_\sigma^\star$	1.0
natural decay rate of *TAF*	$\bar{\lambda}_{decay}^T$	$\lambda_\sigma^\star$	0.001
rate of binding by vessel tips	$\bar{\lambda}_{binding}^T$	$\lambda_\sigma^\star$	0.006
minimum value of *ECM* used in haptotaxis coefficient	$\overline{E}_{mincutoff}^\chi$	$E^\star$, the concentration of ECM secreted by tumor cells	0.1
maximum value of *ECM* used in haptotaxis coefficient	$\overline{E}_{maxcutoff}^\chi$	$\chi_E^\star$	0.9
minimum haptotaxis rate	$\bar{\chi}_{E,\,min}$	$\chi_E^\star E^\star / l^2 \lambda_M$	0.0
maximum haptotaxis rate	$\bar{\chi}_{E,\,max}$	$\chi_E^\star E^\star / l^2 \lambda_M$	0.25
apoptosis rate	A	unit: per day	0
necrosis rate	G_N	unit: per day	0.2
tumor aggresiveness rate	G	unit: per day	26.8
MDE diffusion coefficient	D_M	$\lambda_M \, l^2$, where *l* is the length scale	1.0
production rate of *MDE* by tumor cells	$\bar{\lambda}_{prod.}^M$	λ_M	100.0

Physiological Name	Parameter	Scaled by or Unit	Values
natural decay rate of *MDE*	$\bar{\lambda}_{decay}^{M}$	λ_M	10.0
production rate of *MDE* by vessel tips	$\bar{\lambda}_{spr.prod.}^{M}$	λ_M	1.0
rate of production of *ECM* by tumor cells	$\bar{\lambda}_{prod.}^{E}$	λ_M	2.72
rate of production of *ECM* by vessel tips	$\bar{\lambda}_{spr.prod.}^{E}$	λ_M	0.1
rate of degradation of *ECM* by *MDE*	$\bar{\lambda}_{degradation}^{E}$	$1/M^{\star}$	1.0
minimum value of *ECM* used in mobility coefficient	$\bar{E}_{mincutoff}^{\mu}$	$E^{\star}$	0.0
maximum value of *ECM* used in mobility coefficient	$\bar{E}_{maxcutoff}^{\mu}$	$E^{\star}$	1.0
minimum tumor mobility	$\bar{\mu}_{min}$	$\mu^{\star}$	1.0
maximum tumor mobility	$\bar{\mu}_{max}$	$\mu^{\star}$	4.0